Numerical treatment of small strain single crystal plasticity based on the infeasible primal-dual interior point method

Scheunemann, L.; Nigro, P. S.B.; Schröder, J.

DOI
10.1016/j.ijsolstr.2021.111149

Publication date
2021

Document Version
Final published version

Published in
International Journal of Solids and Structures

International Journal of Solids and Structures 232 (2021) 111149

Contents lists available at ScienceDirect

International Journal of Solids and Structures

journal homepage: www.elsevier.com/locate/ijsolstr

Numerical treatment of small strain single crystal plasticity based on the infeasible primal-dual interior point method

L. Scheunemann [a,*], P.S.B. Nigro [b], J. Schröder [a]

[a] Institut für Mechanik, Fakultät für Ingenieurwissenschaften/Abtl. Bauwissenschaften, Universität Duisburg-Essen, 45141 Essen, Universitätsstr. 15, Germany
[b] Delft Center for Systems and Control (DCSC), TU Delft, Mekelweg 2, 2628 CD Delft, Netherlands

ARTICLE INFO

Article history:
Received 11 February 2021
Received in revised form 20 May 2021
Accepted 28 June 2021
Available online 20 July 2021

Keywords:
Crystal plasticity
Infeasible primal dual interior point method
Nonlinear optimization with constraints
Consistent tangent formulation
Numerical Differentiation
Complex step derivative approximation

ABSTRACT

In this contribution, a small strain single crystal plasticity framework in the context of an infeasible primal–dual interior point method (IPDIPM) is discussed with a focus on the numerical treatment. Related to rate-independent algorithms in the field of single-crystal plasticity, the use of the IPDIPM to solve the constrained optimization problem offers the advantage that it handles the naturally arising redundancy in the slip system intrisically through a barrier term. This formulation penalizes the approach of the unfeasible domain, whereas the penalization term gradually approaches zero in the algorithm. This paper focusses on the numerical treatment and presents different tangent operator formulations and compares their convergency behavior in a numerical example.

1. Introduction

The focus of this paper is the derivation and discussion of algorithmic consistent and numerically derived tangent operators for single crystal plasticity in the framework in a formulation based on the infeasible primal–dual interior point method, which was proposed in Scheunemann et al. (2020).

Since many decades, material modeling of crystalline solids is a field of active research. Therein, the continuum slip theory, see e.g. Mandel (1972), Havner et al. (1982) and references therein, builds the well-established foundation for the phenomenological description of the mechanical response of crystal elasto-plasticity. On the crystallographic lattice, slip systems are defined which are described by their related continuum slip fields. For example, in a face centered cubic (fcc) crystal, these slip systems are associated to the densely packed planes in the atomic lattice, which are eight $\{111\}$ planes in the crystal reference frame. Each slip plane contains three $\langle 110 \rangle$ slip direction leading to a total number of 24 slip systems. In relation to classical plasticity formulations, single crystal plasticity can be recast into the format of multi-surface plasticity, see e.g. Koiter et al. (1960) and Mandel (1972), such that a yield criterion is associated to each slip system. The fundamental problem arising in the field of single crystal plasticity is that, unlike the multisurface plasticity formulations, the yield functions on the slip systems are linearly dependent, which leads to a non-uniqueness of the active slip systems, see e.g. Taylor (1938), Kocks (1970), Havner et al. (1982). There exist several approaches to handle the problem of non-uniqueness, where one class aims at the identification of active slip systems and thereby leads to rate-independent approaches, whereas rate dependent formulations regularize the system of equations by introducing viscosity to the slip rate formulation. Even when an active set of slip systems has been determined, the linear dependency of the slip systems leads to an ill-posed problem in the determination of the slip on the active systems. A brief overview will be given here for the field of rate independent approaches. In this field, Cuitiño and Ortiz (1992), Miehe (1996), Simo et al. (1988) developed algorithms to identify the active sets in different ways. An algorithm successively determining the active set was developed in Borja and Wren (1993) and extended in Borja and Rahmani (2012). In the problem of solving the arising ill-posed problem when determining the slip rates, Anand and Kothari (1996) use a generalized inverse formulation based on singular value decomposition of the Jacobian matrix, which has been extended to an alternative generalized inverse in a reduced space in Schröder and Miehe (1997). Building up on this work, a regularization approach based on a diagonal shift technique was introduced by Miehe and Schröder (2001). With the aim to ensure uniqueness to the problem, Arminjon (1991) proposed an approach using a smoothed yield surface whereas

* Corresponding author.
E-mail address: lisa.scheunemann@uni-due.de (L. Scheunemann).

https://doi.org/10.1016/j.ijsolstr.2021.111149
0020-7683/

Gambin (1992) use a scalar yield condition instead of the classical yield functions. An algorithm based on an augmented Lagrangian formulation based on the principle of maximum dissipation was proposed by Schmidt-Baldassari (2003). McGinty and McDowell (2006) developed a sequential algorithm for rate-independent single crystal plasticity which treats the identification of the active slip systems and the computation of the shearing rates separately. Miehe and Rosato (2007) propose a method for the determination of slip activity in fcc crystals based on a pure geometric setup of the slip systems and a fully implicit update strategy based on the consistency condition was presented by Zuo (2011). Recently, a formulation for small strain single crystal plasticity based on the infeasible primal–dual interior point method was proposed in Scheunemann et al. (2020). Among several works who discuss and extend the developed algorithms, Busso and Cailletaud (2005) compared different algorithms under multiaxial loading paths. Prüger and Kiefer (2020) have discussed several formulations in detail and evaluated their behavior in non-monotonous loading scenarios and for anisotropic hardening relations.

As mentioned above, rate-dependent formulations are utilized frequently to overcome the issues on non-uniqueness imposed by the rate independent formulations. The viscous regularization based on power-type creep laws, as discussed in e.g. Asaro and Rice (1977), Asaro (1983), Peirce et al. (1982), Steinmann and Stein (1996) and Mathur and Dawson (1989), circumvents the active set search and all slip systems are considered to be active simultaneously. A numerically robust implementation is provided in the simulation framework *Damask*, see e.g. Roters et al. (2010) and Shanthraj et al. (2015). The sensitivity of these algorithms in anisotropic hardening scenarios with respect to a small misorientation of the initial crystal orientation is discussed in Prüger and Kiefer (2020), who point out that the rate independent formulation and its description as a limit of the rate dependent case, i.e. vanishing viscosity, does not necessarily yield similar results. A focus of current research is the field of strain gradient plasticity, which considers a contribution to the energy from geometrically necessary dislocation, see e.g. Gurtin (2000), Reddy et al. (2012), Gurtin et al. (2007), Forest and Gueninchault (2013), Wulfinghoff and Böhlke (2013), Wulfinghoff and Böhlke (2015) and Lewandowski and Stupkiewicz (2018), among other, however, this topic is not in the scope of the presented work.

The notion of consistent algorithmic elastoplastic tangent moduli is well-known for a discrete algorithmic problem when applying a Newton–Raphson scheme. The algorithmic consistent elastoplastic moduli, which produce the exact Hessian of the discrete problem, can be derived from the incremental stress state with respect to the incremental strains. Many works, see e.g. Simo (1998), Blaheta (1997) state the presenvance of quadratic convergence properties of the Newton scheme for the iterative solution of the initial boundary value problem in elastoplasticity. However, Sauter and Wieners (2011) point out that the complexity of the formulation rises when treating multi-yield phenomena compared to single yield phenomena and nonsmoothness is observed for rate-independent algorithms where convergence properties cannot be deduced from standard Newton theory. The authors show superlinear convergence for a Drucker-Prager type elastoplasticity in the context of semismooth Newton methods. For simple associated plasticity models, convergency properties are shown in Alberty et al. (1999), whereas Blaheta (1997) shows quadratic convergence for a correctly identified set of active constraints in multisurface plasticity. In the field of single crystal plasticity, Miehe and Schröder (2001) provide a consistent algorithmic tangent operator for a rate-independent formulation, also Prüger and Kiefer (2020) provide such operators for different algorithms. As an alternative to the algebraic derivation of algorithmic consistent tangent operator based on the incremental stress strain relationship, numerical differentiation schemes can be applied. Beside the well-known finite difference scheme, the complex-step derivative approximation, which uses a Taylor series expansion along the imaginary axis, has become more and more popular in the last years due to the robustness with respect to the size of the applied perturbation. A discussion of numerical tangent operators for localization analysis can be found in Hürkamp et al. (2015), Tanaka et al. (2014) analyze different tangent operator formulations for viscoelasticity. An incremental variational formulation based on hyper-dual numbers can be found in Tanaka et al. (2016).

The focus of this paper is the derivation and discussion of an algorithmic consistent tangent operator and its comparison to numerically derived tangent operators for single crystal plasticity in the framework in a formulation based on the infeasible primal–dual interior point method, which was proposed in Scheunemann et al. (2020). The framework of small strain single crystal plasticity in the framework of the infeasible primal–dual interior point method is recapitulated first, before the tangent operators are introduced. In numerical examples, the comparison of the convergence is discussed and the orientation specific anisotropy and resulting shear band evolution is shown.

2. Constitutive framework of single crystal plasticity at small strains

The classical description of the constitutive behavior of face centered cubic (fcc) single crystals at small strains is given in the following. The elastic material behavior is assumed to be governed by the free energy function

$$\psi^{\mathrm{e}} = \frac{1}{2}\boldsymbol{\varepsilon}^{\mathrm{e}} : \mathbb{C}^{\mathrm{e}} : \boldsymbol{\varepsilon}^{\mathrm{e}} \qquad \text{with} \qquad \boldsymbol{\varepsilon}^{\mathrm{e}} = \boldsymbol{\varepsilon} - \boldsymbol{\varepsilon}^{\mathrm{p}}, \tag{1}$$

where $\boldsymbol{\varepsilon}^{\mathrm{e}}$ describes the elastic part of the strains and $\boldsymbol{\varepsilon}^{\mathrm{p}}$ describes the plastic part. Here, the general anisotropic linear elastic response formulation is governed by the fourth-order tensor $\mathbb{C}^{\mathrm{e}}$ of elasticity moduli. For an application to fcc crystals, we consider cubic elastic symmetry with

$$\mathbb{C}^{\mathrm{e}} = \mathbb{C}^{\mathrm{e}\,ijkl}\boldsymbol{e}_i \otimes \boldsymbol{e}_j \otimes \boldsymbol{e}_k \otimes \boldsymbol{e}_l \tag{2}$$

in the cartesian base $\{\boldsymbol{e}_i\}_{i=1,3}$ aligned to the cubic crystal. Based on the above defined elastic free energy, the Cauchy stress is defined as

$$\boldsymbol{\sigma} = \frac{\partial \psi^{e}}{\partial \boldsymbol{\varepsilon}^{e}} = \mathbb{C}^{\mathrm{e}} : \boldsymbol{\varepsilon}^{\mathrm{e}}. \tag{3}$$

In crystal plasticity, the plastic behavior of the material is governed by the anisotropic response from the crystalline structure. Therein, a certain number of slip systems $\alpha \in 1 \dots m$ is defined, which are described by the slip direction $\boldsymbol{m}^{\alpha}$ and the slip system normal $\boldsymbol{n}^{\alpha}$. For fcc crystals, these slip systems form an octahedral shape, see Fig. 1a for an illustration and a total number of $2 \times N$ slip systems, $N = 12$, can be defined. The definition of the first 12 slip systems is given in Fig. 1b, where for slip system $N+1$, it holds that $\boldsymbol{m}^{N+1} = -\boldsymbol{m}^{N}$. The plastic slip on each slip system is described by γ^{α}, whereas it must hold that $\dot{\gamma}^{\alpha} \geqslant 0$, which is related to the rate of the plastic part of the small strain tensor by

$$\dot{\boldsymbol{\varepsilon}}^{\mathrm{p}} = \sum_{\alpha=1}^{N} \boldsymbol{P}^{\alpha}\dot{\gamma}^{\alpha}, \qquad \boldsymbol{P}^{\alpha} = \mathrm{sym}(\boldsymbol{m}^{\alpha} \otimes \boldsymbol{n}^{\alpha}), \tag{4}$$

where $\boldsymbol{P}^{\alpha}$ is a projection tensor related to slip system α.

It has been observed in metals that plastic deformation on a slip system only occurs when the stress level exceeds a certain limit value, which justifies the definition of yield surfaces

$$\phi^{\alpha} := \tau^{\alpha} - g^{\alpha} \leqslant 0, \quad \text{where} \quad g^{\alpha}(t=0) = \tau_0 \tag{5}$$

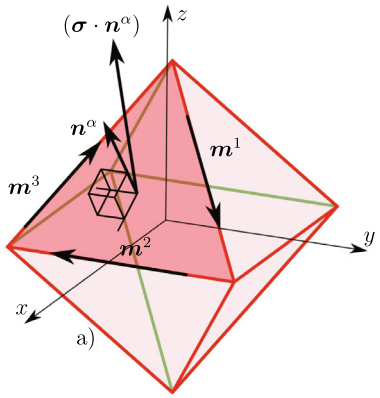

b)

α	$\boldsymbol{m}^\alpha$	$\boldsymbol{n}^\alpha$	α	$\boldsymbol{m}^\alpha$	$\boldsymbol{n}^\alpha$
1	[0 1 -1]	(1 1 1)	7	[0 1 1]	(-1 1 -1)
2	[-1 0 1]	(1 1 1)	8	[1 0 -1]	(-1 1 -1)
3	[1 -1 0]	(1 1 1)	9	[-1 -1 0]	(-1 1 -1)
4	[0 1 -1]	(-1 1 1)	10	[0 1 1]	(1 1 -1)
5	[1 0 1]	(-1 1 1)	11	[1 -1 0]	(1 1 -1)
6	[-1 -1 0]	(-1 1 1)	12	[1 0 1]	(1 1 -1)

Fig. 1. (a) Octahedral arrangement of slip planes in fcc crystal unitcell. (b) Summary of slip systems of face centered cubic unitcell with numbering given by α and slip normal- and slip direction vector given by $\boldsymbol{n}^\alpha$ and $\boldsymbol{m}^\alpha$, respectively. Taken from Scheunemann et al. (2020).

wherein the resolved shear stress on the slip system is described by $\tau^\alpha = \boldsymbol{\sigma} : \boldsymbol{P}^\alpha$ and the yield stress is given by g^α with τ_0 as the intial yield stress. For each slip system, the Karush-Kuhn Tucker conditions

$$\dot{\gamma}^\alpha \geqslant 0, \quad \Phi^\alpha \leqslant 0, \quad \Phi^\alpha \dot{\gamma}^\alpha = 0 \tag{6}$$

must hold. g^α can be understood as a work conjugate to the plastic slip, related through an idealized energy storage mechanism governed by a plastic potential ψ^p, i.e.,

$$g^\alpha = \frac{\partial \psi^p}{\partial \gamma^\alpha}. \tag{7}$$

In e.g. Ortiz and Stainier (1999), suitable approximations are given for plastic stored energy functions. For nonlinear hardening models, however, this description based on a plastic potential is in general not possible and a classical rate form

$$\dot{g}^\alpha = \sum_\beta h^{\alpha\beta} \dot{\gamma}^\beta \tag{8}$$

can be defined, where $h^{\alpha\beta}$ are the hardening moduli. In this work, the classical assumption

$$h^{\alpha\beta} = \hat{h}(A)\left[q + (1-q)\delta^{\alpha\beta}\right], \tag{9}$$

is used, as suggested in Hutchinson (1976) and Peirce et al. (1982). Therein, the strain-like interal variable A is given by

$$A = \sum_\alpha \gamma^\alpha, \tag{10}$$

and describes the interal hardening state of the single crystal by the sum of accumulated slips on all slip systems. The type of hardening behavior in this model is described by the parameter $q \in [1, 1.4]$, which was experimentally investigated in Kocks (1970) for fcc crystals. A value of $q = 1$ describes isotropic (Taylor-type) hardening. For the scalar-valued function $\hat{h}(A)$, different forms have been proposed in the literature, see e.g. Chang and Asaro (1981).

The evolution of $\boldsymbol{\varepsilon}^p$ takes place according to the principle of maximum dissipation, such that for ideal plastic behavior, using Eq. (3) and (4),

$$\mathscr{D}_{\text{red}} = \boldsymbol{\sigma} : \dot{\boldsymbol{\varepsilon}}^p = \sum_\alpha \boldsymbol{P}^\alpha : \mathbb{C}^{\text{e}} : \boldsymbol{\varepsilon}^{\text{e}} \dot{\gamma}^\alpha \tag{11}$$

and taking into account hardening effects

$$\mathscr{D}_{\text{red}} = \boldsymbol{\sigma} : \dot{\boldsymbol{\varepsilon}}^p - \sum_\alpha g^\alpha \dot{\gamma}^\alpha = \sum_\alpha \left(\boldsymbol{P}^\alpha : \mathbb{C}^{\text{e}} : \boldsymbol{\varepsilon}^{\text{e}} - g^\alpha\right) : \dot{\gamma}^\alpha \tag{12}$$

needs to be maximized under consideration of the yield condition, see Eq. (5). This leads to the constrained optimization problem

$$\begin{aligned} &\text{maximize} && \mathscr{D}_{\text{red}}\left(\dot{\gamma}^\alpha\right) \\ &\text{subject to} && \Phi^\alpha \leqslant 0 \ \text{ for } \ \alpha = 1, 2, \ldots, N, \\ &\text{subject to} && \dot{\gamma}^\alpha \geqslant 0 \ \text{ for } \ \alpha = 1, 2, \ldots, N. \end{aligned} \tag{13}$$

The stated optimization problem in Eq. (13) can be treated using different methods. The construction of a Lagrange functional leads to a classical rate independent formulation, which has well-known difficulties: The active set of slip systems need to be determined, which requires to solve an ill-conditioned problem. The determination of the slip rates from the active systems is not unique due to the redundancy in the constraint conditions. Perturbation techniques or the generalized inverse techniques can be used to overcome these difficulties. Other approaches include penalty formulations, which regularize the formulation but, however, only fulfill the constraint conditions in an approximate manner. An augmented Lagrangian formulation was proposed in Schmidt-Baldassari (2003). Here, the constrained optimization problem is treated using the infeasible primal–dual interior point method, in analogy to the formulation introduced in Scheunemann et al. (2020), where details on the formulation can be found. A brief introduction of the infeasible primal–dual interior point method is given in the next section.

3. Infeasible primal–dual interior point method for single crystal plasticity

As defined in the last section, the considered problem is the maximum dissipation constrained by flow criteria and values of plastic slip rates higher than zero. This is equivalent to a nonlinear optimization problem with multiple inequality-constraints

$$\begin{aligned} &\text{min} && -\mathscr{D}_{\text{red}}(\dot{\boldsymbol{\gamma}}) && \forall && -\mathscr{D}_{\text{red}}(\dot{\boldsymbol{\gamma}}) \in \mathbb{R}_-, \\ &\text{subject to} && \boldsymbol{\phi} \leqslant \boldsymbol{0} && \forall && \boldsymbol{\phi}(\boldsymbol{\gamma}) \in \mathbb{R}^m, \\ &\text{with} && \dot{\boldsymbol{\gamma}} \geqslant \boldsymbol{0} && \forall && \dot{\boldsymbol{\gamma}} \in \mathbb{R}^m_+. \end{aligned} \tag{14}$$

To implement the infeasible primal–dual interior point method, based on the work in Scheunemann et al. (2020) and Nigro et al. (2019), the addition of slack variables is necessary to transfer inequality constraints to equality constraints, leading to the alternative formulation of the optimization problem in Eq. (14)

$$\begin{aligned} &\min \quad -\mathscr{D}_{\text{red}}(\dot{\boldsymbol{\gamma}}), \\ &\text{subject to} \quad \boldsymbol{\phi} + \boldsymbol{s} = \boldsymbol{0}, \\ &\text{with} \quad \dot{\boldsymbol{\gamma}} \geqslant \boldsymbol{0} \quad \text{and} \quad \boldsymbol{s} \geqslant \boldsymbol{0}. \end{aligned} \tag{15}$$

Now, the problem replaces the more complex inequality in Eq. (14.2) by two simple inequalities in Eq. (15.3). To deal with these inequalities, a continuous, differentiable, and smooth approach is applied to ensure a limitation in the domain. Such an approach is called barrier function. Then, based on the simple inequalities, two barrier functions are required

$$\begin{aligned} &\min -\mathscr{D}_{\text{red}}(\dot{\boldsymbol{\gamma}}) - \mu \sum_{i=1}^{m} \ln(s_i) - \mu \sum_{i=1}^{m} \ln(\dot{\gamma}_i) \quad \forall \quad \mu \in \mathbb{R}_+ \\ &\text{subject to} \quad \boldsymbol{\phi} + \boldsymbol{s} = \boldsymbol{0} \quad \forall \quad \boldsymbol{s} \in \mathbb{R}^m_+ \\ &\boldsymbol{s}^T = [s_1, \dots, s_m] \quad \forall \quad s_i \in \mathbb{R}_+ \\ &\boldsymbol{s} = \boldsymbol{S}\boldsymbol{e}_m \quad \forall \quad \boldsymbol{S} = \text{diag}(\boldsymbol{s}) \in \mathbb{R}^{m \times m} \end{aligned} \tag{16}$$

with m as the number of slip systems. Based on the mentioned steps, the Lagrangian function is set up as

$$\begin{aligned} l(\dot{\boldsymbol{\gamma}}, \boldsymbol{\lambda}, \boldsymbol{s}) = &-\mathscr{D}_{\text{red}}(\dot{\boldsymbol{\gamma}}) + \boldsymbol{\lambda}^T[\boldsymbol{\phi} + \boldsymbol{s}] - \mu \sum_{i=1}^{m} \ln(s_i) \\ &- \mu \sum_{i=1}^{m} \ln(\dot{\gamma}_i) \quad \forall\, l \in \mathbb{R} \text{ and } \boldsymbol{\lambda} \in \mathbb{R}^m_+ \end{aligned} \tag{17}$$

$$\text{with} \quad \boldsymbol{\lambda}^T = [\lambda_1, \dots, \lambda_m] \quad \forall \quad \lambda_i \in \mathbb{R}_+ \tag{18}$$

$$\text{and} \quad \boldsymbol{\lambda} = \boldsymbol{\Lambda}\boldsymbol{e}_m \quad \forall \quad \boldsymbol{\Lambda} = \text{diag}(\boldsymbol{\lambda}) \in \mathbb{R}^{m \times m}. \tag{19}$$

Please note that the same barrier parameter μ is used here for the two barrier functions. A consideration of two separate barrier parameters and an independent reduction during the local iteration may lead to a stagnation in the problem, compare Hinder and Ye (2018). Next, it is possible to consider the classical Kuhn-Tucker condition

$$\lambda_i \geqslant 0, \quad \phi(\boldsymbol{\gamma})_i \leqslant 0 \quad \text{and} \quad \lambda_i \, \phi(\boldsymbol{\gamma})_i = 0. \tag{20}$$

Related to the formulation, the gradients are defined by

$$\frac{\partial l}{\partial \dot{\boldsymbol{\gamma}}} = -\frac{\partial \mathscr{D}_{\text{red}}}{\partial \dot{\boldsymbol{\gamma}}} + \frac{\partial \boldsymbol{\phi}^T}{\partial \dot{\boldsymbol{\gamma}}} \boldsymbol{\lambda} - \mu \dot{\boldsymbol{\Gamma}}^{-1} \boldsymbol{e}_m \tag{21}$$

$$\frac{\partial l}{\partial \boldsymbol{\lambda}} = \boldsymbol{\phi} + \boldsymbol{s}, \tag{22}$$

$$\frac{\partial l}{\partial \boldsymbol{s}} = \boldsymbol{\lambda} - \mu \boldsymbol{S}^{-1} \boldsymbol{e}_m, \tag{23}$$

$$\text{with } \dot{\boldsymbol{\Gamma}} = \text{diag}(\dot{\boldsymbol{\gamma}}) \in \mathbb{R}^{m \times m} \quad \text{and} \quad \frac{\partial l}{\partial \dot{\boldsymbol{\gamma}}}, \frac{\partial \mathscr{D}_{\text{red}}}{\partial \dot{\boldsymbol{\gamma}}} \in \mathbb{R}^m, \frac{\partial \boldsymbol{\phi}}{\partial \dot{\boldsymbol{\gamma}}} \in \mathbb{R}^{m \times m}.$$

For algebraic simplification, the gradient in Eq. (23) can be replaced by

$$\frac{\partial \tilde{l}}{\partial \boldsymbol{s}} = \boldsymbol{S} \frac{\partial l}{\partial \boldsymbol{s}} = \boldsymbol{S}\boldsymbol{\lambda} - \mu \boldsymbol{e}_m. \tag{24}$$

The set of nonlinear equations given in Eq. (21), Eq. (22) and Eq. (23) must be equated to zero. The system of equations is linearized using Taylor series expansion, ignoring terms of second and higher order and set the equation to zero, leading to

$$\begin{aligned} \boldsymbol{0} &= \tfrac{\partial l}{\partial \dot{\boldsymbol{\gamma}}} + \tfrac{\partial^2 l}{\partial \dot{\boldsymbol{\gamma}}^2} \Delta\dot{\boldsymbol{\gamma}} + \tfrac{\partial^2 l}{\partial \dot{\boldsymbol{\gamma}} \partial \boldsymbol{\lambda}} \Delta\boldsymbol{\lambda} + \tfrac{\partial^2 l}{\partial \dot{\boldsymbol{\gamma}} \partial \boldsymbol{s}} \Delta\boldsymbol{s}, \\ \boldsymbol{0} &= \tfrac{\partial l}{\partial \boldsymbol{\lambda}} + \tfrac{\partial^2 l}{\partial \boldsymbol{\lambda} \partial \dot{\boldsymbol{\gamma}}} \Delta\dot{\boldsymbol{\gamma}} + \tfrac{\partial^2 l}{\partial \boldsymbol{\lambda}^2} \Delta\boldsymbol{\lambda} + \tfrac{\partial^2 l}{\partial \boldsymbol{\lambda} \partial \boldsymbol{s}} \Delta\boldsymbol{s}, \\ \boldsymbol{0} &= \tfrac{\partial l}{\partial \boldsymbol{s}} + \tfrac{\partial^2 l}{\partial \boldsymbol{s} \partial \dot{\boldsymbol{\gamma}}} \Delta\dot{\boldsymbol{\gamma}} + \tfrac{\partial^2 l}{\partial \boldsymbol{s} \partial \boldsymbol{\lambda}} \Delta\boldsymbol{\lambda} + \tfrac{\partial^2 l}{\partial \boldsymbol{s}^2} \Delta\boldsymbol{s}. \end{aligned} \tag{25}$$

Arranging Eq. (25) in matrix form and using the explicit values yields

$$\begin{bmatrix} -\frac{\partial^2 \mathscr{D}_{\text{red}}}{\partial \dot{\boldsymbol{\gamma}}^2} + \frac{\partial^2 \boldsymbol{\phi}}{\partial \dot{\boldsymbol{\gamma}}^2}\boldsymbol{\lambda} + \mu \dot{\boldsymbol{\Gamma}}^{-2} & \frac{\partial \boldsymbol{\phi}^T}{\partial \dot{\boldsymbol{\gamma}}} & \boldsymbol{O}_m \\ \frac{\partial \boldsymbol{\phi}}{\partial \dot{\boldsymbol{\gamma}}} & \boldsymbol{O}_m & \boldsymbol{I}_m \\ \boldsymbol{O}_m & \boldsymbol{S} & \boldsymbol{\Lambda} \end{bmatrix} \begin{bmatrix} \Delta\dot{\boldsymbol{\gamma}} \\ \Delta\boldsymbol{\lambda} \\ \Delta\boldsymbol{s} \end{bmatrix} = \begin{bmatrix} -\frac{\partial \mathscr{D}_{\text{red}}}{\partial \dot{\boldsymbol{\gamma}}} - \frac{\partial \boldsymbol{\phi}}{\partial \dot{\boldsymbol{\gamma}}}\boldsymbol{\lambda} + \mu \dot{\boldsymbol{\Gamma}}^{-1} \boldsymbol{e}_m \\ -\boldsymbol{\phi} - \boldsymbol{s} \\ -\boldsymbol{S}\boldsymbol{\lambda} + \mu \boldsymbol{e}_m \end{bmatrix}. \tag{26}$$

The second and third line of Eq. (26) can be reformulated such that the increment $\Delta\boldsymbol{s}$ can be expressed in terms of the increment of Lagrange multiplier $\Delta\boldsymbol{\lambda}$ and a reduction of the system size is achieved. Hence, with the increment of the slack variable given as

$$\Delta\boldsymbol{s} = -\boldsymbol{\Lambda}^{-1}\boldsymbol{S}\boldsymbol{\lambda} + \mu\boldsymbol{\Lambda}^{-1}\boldsymbol{e}_m - \boldsymbol{\Lambda}^{-1}\boldsymbol{S}\Delta\boldsymbol{\lambda}, \tag{27}$$

the final system follows with respect to the two variables $\dot{\boldsymbol{\gamma}}$ and $\boldsymbol{\lambda}$

$$\begin{bmatrix} \frac{\partial^2 \mathscr{D}_{\text{red}}}{\partial \dot{\boldsymbol{\gamma}}^2} + \frac{\partial^2 \boldsymbol{\phi}}{\partial \dot{\boldsymbol{\gamma}}^2}\boldsymbol{\lambda} + \mu \dot{\boldsymbol{\Gamma}}^{-2} & \frac{\partial \boldsymbol{\phi}^T}{\partial \dot{\boldsymbol{\gamma}}} \\ \frac{\partial \boldsymbol{\phi}}{\partial \dot{\boldsymbol{\gamma}}} & -\boldsymbol{\Lambda}^{-1}\boldsymbol{S} \end{bmatrix} \begin{bmatrix} \Delta\dot{\boldsymbol{\gamma}} \\ \Delta\boldsymbol{\lambda} \end{bmatrix} = \begin{bmatrix} -\frac{\partial \mathscr{D}_{\text{red}}}{\partial \dot{\boldsymbol{\gamma}}} - \frac{\partial \boldsymbol{\phi}}{\partial \dot{\boldsymbol{\gamma}}}\boldsymbol{\lambda} + \mu \dot{\boldsymbol{\Gamma}}^{-1} \boldsymbol{e}_m \\ -\boldsymbol{\phi} - \mu\boldsymbol{\Lambda}^{-1}\boldsymbol{e}_m \end{bmatrix}. \tag{28}$$

and the increment of the slack variable from Eq. (27)

$$\Delta\boldsymbol{s} = -\boldsymbol{\Lambda}^{-1}\boldsymbol{S}\Delta\boldsymbol{\lambda} - \boldsymbol{s} + \mu\boldsymbol{\Lambda}^{-1}\boldsymbol{e}_m. \tag{29}$$

In the matrix of Eq. (28), the penalization term can generate unstable values, which lead in some cases to matrix singularity. Another problem is the lack of control of the KKT condition related to the primal variable $\dot{\boldsymbol{\gamma}}$. To deal with these two problems, the dual variable of the variable $\dot{\boldsymbol{\gamma}}$ is defined through the derivative of the barrier function related to $\dot{\boldsymbol{\gamma}}$, such that

$$\boldsymbol{\rho}_\gamma = \frac{\partial \left[\mu \sum_{i=1}^{m} \ln(\dot{\gamma}_i) \right]}{\partial \dot{\boldsymbol{\gamma}}} \quad \Longleftrightarrow \quad \boldsymbol{\rho}_\gamma = \mu \dot{\boldsymbol{\Gamma}}^{-1} \boldsymbol{e}_m \quad \text{or} \quad \dot{\boldsymbol{\Gamma}}\boldsymbol{\rho}_\gamma = \mu \boldsymbol{e}_m \tag{30}$$

$$\boldsymbol{\Theta}_\gamma = \text{diag}\left(\boldsymbol{\rho}_\gamma\right) \in \mathbb{R}^{m \times m} \quad \text{and} \quad \dot{\boldsymbol{\Gamma}} = \text{diag}(\dot{\boldsymbol{\gamma}}) \in \mathbb{R}^{m \times m} \tag{31}$$

$$\boldsymbol{\rho}_\gamma = \boldsymbol{\Theta}_\gamma \boldsymbol{e}_m \in \mathbb{R}^m_+ \quad \text{and} \quad \dot{\boldsymbol{\gamma}} = \dot{\boldsymbol{\Gamma}} \boldsymbol{e}_m \in \mathbb{R}^m_+. \tag{32}$$

As explained previously, with the dual variable of $\dot{\boldsymbol{\gamma}}$, it is possible to control the penalization of $\dot{\boldsymbol{\gamma}}$. Related to the instability of the penalization term in Eq. (28), it is possible to mitigate this problem with the second derivative of Eq. (30), which yields

$$\frac{\partial \boldsymbol{\rho}_\gamma}{\partial \dot{\boldsymbol{\gamma}}} = -\mu \dot{\boldsymbol{\Gamma}}^{-2} \quad \text{but} \quad \boldsymbol{\Theta}_\gamma = \mu \dot{\boldsymbol{\Gamma}}^{-1} \tag{33}$$

$$\frac{\partial \boldsymbol{\rho}_\gamma}{\partial \dot{\boldsymbol{\gamma}}} = -\boldsymbol{\Theta}_\gamma \dot{\boldsymbol{\Gamma}}^{-1} \tag{34}$$

with the first derivative of the dual variable of $\dot{\boldsymbol{\gamma}}$, the increment of Eq. (30) is approximated by

$$\Delta\boldsymbol{\rho}_\gamma \simeq \tfrac{\partial \boldsymbol{\rho}_\gamma}{\partial \dot{\boldsymbol{\gamma}}} \Delta\dot{\boldsymbol{\gamma}} \tag{35}$$

$$\Delta\boldsymbol{\rho}_\gamma \simeq -\boldsymbol{\Theta}_\gamma \dot{\boldsymbol{\Gamma}}^{-1} \Delta\dot{\boldsymbol{\gamma}} \tag{36}$$

and finally, the update of Eq. (30) is deduced by

$$\boldsymbol{\rho}_\gamma + \Delta\boldsymbol{\rho}_\gamma \simeq \mu \dot{\boldsymbol{\Gamma}}^{-1} \boldsymbol{e}_m - \boldsymbol{\Theta}_\gamma \dot{\boldsymbol{\Gamma}}^{-1} \Delta\dot{\boldsymbol{\gamma}} \tag{37}$$

$$\Delta\boldsymbol{\rho}_\gamma \simeq \mu \dot{\boldsymbol{\Gamma}}^{-1} \boldsymbol{e}_n - \boldsymbol{\Theta}_\gamma \dot{\boldsymbol{\Gamma}}^{-1} \Delta\dot{\boldsymbol{\gamma}} - \boldsymbol{\rho}_\gamma \tag{38}$$

The approximation described in Eq. (38) is applied in the matrix diagonal of Eq. (28) and results in a numerical behaviour similar to a pertubation approach. Lastly, the final system in the matricial form becomes

$$\begin{bmatrix} -\frac{\partial^2 \mathscr{D}_{\text{red}}}{\partial \dot{\gamma}^2} + \frac{\partial^2 \phi}{\partial \dot{\gamma}^2}\lambda - \Theta_\gamma \dot{\Gamma}^{-1} & \frac{\partial \phi}{\partial \dot{\gamma}}^T \\ \frac{\partial \phi}{\partial \dot{\gamma}} & -\Lambda^{-1} S \end{bmatrix} \begin{bmatrix} \Delta\dot{\gamma} \\ \Delta\lambda \end{bmatrix} = \begin{bmatrix} -\frac{\partial \mathscr{D}_{\text{red}}}{\partial \dot{\gamma}} - \frac{\partial \phi}{\partial \dot{\gamma}}\lambda + \mu \dot{\Gamma}^{-1} e_m \\ -\phi - \mu \Lambda^{-1} e_m \end{bmatrix}. \tag{39}$$

An alternative derivation of this formulation from the barrier problem can be found in the Appendix A.2.

4. Time integration algorithm

Based on the infeasible primal–dual interior point method (IPDIPM) described in the last section and presented in detail in Scheunemann et al. (2020), a time integration algorithm for the evolution problem will be discussed in the following. For the sake of brevity, a reduced notation as described in Scheunemann et al. (2020) will be used throughout the remaining part of the paper. Therein, a transition from tensorial notation to matrix notation is made.

For the evolution of the plastic strains, respectively the plastic slip rate, a time region of interest $[0, T]$ is considered, with

$$[0, T] = \cup_{n+1}^{N} [t_n, t_{n+1}] \tag{40}$$

considering a typical time interval $[t_n, t_{n+1}]$ in the following. The time discrete formulation of the reduced dissipation inequality, see Eq. (13) yields

$$\mathscr{D}_{\text{red}}(\Delta\gamma^\alpha_{n+1}) = \sum_\alpha \left(\boldsymbol{P}^\alpha : \mathbb{C}^{\text{e}} : \boldsymbol{\varepsilon}_{n+1} - \sum_\beta \boldsymbol{P}^\alpha : \mathbb{C}^{\text{e}} : \boldsymbol{P}^\beta \gamma^\beta_{n+1} - g^\alpha_{n+1} \right) \Delta\gamma^\alpha_{n+1} \geqslant 0. \tag{41}$$

where an implicit backward Euler scheme is used for the integration of the continuous variables. All variables at t_n are assumed to be known and for simplicity purpose, the subscript index $n+1$ is omitted, such that all variables without index denote the evaluation at the current time t_{n+1}. As initial conditions at $t = 0$, we assume $\boldsymbol{\gamma}$ to be zero and $g^\alpha = \tau_0 \quad \forall \quad \alpha = 1, 2, \dots m$. In view of the application of interior point method according to Eq. (39), the derivatives of the objective function with respect to $\Delta\boldsymbol{\gamma}$ will be given in detail in the following. The derivation leads to

$$\begin{aligned} \frac{\partial \mathscr{D}_{\text{red}}}{\partial \Delta\gamma} &= \frac{\partial}{\partial \Delta\gamma}\left[\underline{\boldsymbol{\varepsilon}}^{\text{e,trial}^{\text{T}}} \underline{\mathbb{C}}^{\text{e}} \underline{\boldsymbol{P}} \Delta\boldsymbol{\gamma}\right] + \frac{\partial}{\partial \Delta\gamma}\left[-\Delta\boldsymbol{\gamma}^T \underline{\boldsymbol{P}}^T \underline{\mathbb{C}}^{\text{e}} \underline{\boldsymbol{P}} \Delta\boldsymbol{\gamma}\right] + \frac{\partial}{\partial \Delta\gamma}\left[-\boldsymbol{g}\Delta\boldsymbol{\gamma}\right] \\ &= \underline{\boldsymbol{P}}^T \underline{\mathbb{C}}^{\text{e}} \underline{\boldsymbol{\varepsilon}}^{\text{e,trial}} - 2\underline{\boldsymbol{P}}^T \underline{\mathbb{C}}^{\text{e}} \underline{\boldsymbol{P}} \Delta\boldsymbol{\gamma} - \boldsymbol{g} - \frac{\partial \boldsymbol{g}}{\partial \Delta\gamma}\Delta\boldsymbol{\gamma} \\ &= \underline{\boldsymbol{P}}^T \underline{\mathbb{C}}^{\text{e}} \underline{\boldsymbol{\varepsilon}}^{\text{e,trial}} - 2\underline{\boldsymbol{P}}^T \underline{\mathbb{C}}^{\text{e}} \underline{\boldsymbol{P}} \Delta\boldsymbol{\gamma} + \boldsymbol{h}(\Delta\boldsymbol{\gamma}) \end{aligned} \tag{42}$$

with $\frac{\partial \mathscr{D}_{\text{red}}}{\partial \Delta\gamma} \in \mathbb{R}^m$. The trial elastic strain measure $\underline{\boldsymbol{\varepsilon}}^{\text{e,trial}}$ is defined by $\underline{\boldsymbol{\varepsilon}}^{\text{e,trial}} = \underline{\boldsymbol{\varepsilon}}_{n+1} - \underline{\boldsymbol{\varepsilon}}^{\text{p}}_n$. The second derivative leads to

$$\begin{aligned} \frac{\partial^2 \mathscr{D}_{\text{red}}}{\partial \Delta\gamma^2} &= \frac{\partial}{\partial \Delta\gamma}\left[\underline{\boldsymbol{P}}^T \underline{\mathbb{C}}^{\text{e}} \underline{\boldsymbol{\varepsilon}}^{\text{e,trial}}\right] + \frac{\partial}{\partial \Delta\gamma}\left[-2\underline{\boldsymbol{P}}^T \underline{\mathbb{C}}^{\text{e}} \underline{\boldsymbol{P}} \Delta\boldsymbol{\gamma}\right] + \frac{\partial}{\partial \Delta\gamma}\left[-\frac{\partial \boldsymbol{g}}{\partial \Delta\gamma}\Delta\boldsymbol{\gamma} - \boldsymbol{g}\right] \\ &= -2\underline{\boldsymbol{P}}^T \underline{\mathbb{C}}^{\text{e}} \underline{\boldsymbol{P}} - \frac{\partial^2 \boldsymbol{g}}{\partial \Delta\gamma^2}\Delta\boldsymbol{\gamma} - 2\frac{\partial \boldsymbol{g}}{\partial \Delta\gamma} \\ &= -2\underline{\boldsymbol{P}}^T \underline{\mathbb{C}}^{\text{e}} \underline{\boldsymbol{P}} + \boldsymbol{H}(\Delta\boldsymbol{\gamma}). \end{aligned} \tag{43}$$

We define the functions related to derivatives of the slip resistance function

$$\boldsymbol{h}(\Delta\boldsymbol{\gamma}) = -\frac{\partial \boldsymbol{g}}{\partial \Delta\boldsymbol{\gamma}}\Delta\boldsymbol{\gamma} - \boldsymbol{g}, \tag{44}$$

see Eq. (42) and

$$\boldsymbol{H}(\Delta\boldsymbol{\gamma}) = -\frac{\partial^2 \boldsymbol{g}}{\partial \Delta\boldsymbol{\gamma}^2}\Delta\boldsymbol{\gamma} - 2\frac{\partial \boldsymbol{g}}{\partial \Delta\boldsymbol{\gamma}} \tag{45}$$

related to Eq. (43). The constraint function, as defined in Eq. (5) written in matrix notation is denoted by

$$\boldsymbol{\Phi} = \underline{\boldsymbol{P}}^T \underline{\boldsymbol{\sigma}} - \boldsymbol{g} \tag{46}$$

with the Cauchy stresses in Voigt notation given by

$$\underline{\boldsymbol{\sigma}} = \underline{\mathbb{C}}^{\text{e}}\left[\underline{\boldsymbol{\varepsilon}}^{\text{e,trial}} - \underline{\boldsymbol{P}}\Delta\boldsymbol{\gamma}\right]. \tag{47}$$

Eq. (47) inserted into Eq. (46) leads to

$$\boldsymbol{\Phi} = \underline{\boldsymbol{P}}^T \underline{\mathbb{C}}^{\text{e}}\left[\underline{\boldsymbol{\varepsilon}}^{\text{e,trial}} - \underline{\boldsymbol{P}}\Delta\boldsymbol{\gamma}\right] - \boldsymbol{g}, \tag{48}$$

with the according first and second derivative

$$\frac{\partial \boldsymbol{\Phi}}{\partial \Delta\boldsymbol{\gamma}} = -\underline{\boldsymbol{P}}^{\text{T}} \underline{\mathbb{C}}^{\text{e}} \underline{\boldsymbol{P}} - \frac{\partial \boldsymbol{g}}{\partial \Delta\boldsymbol{\gamma}} \tag{49}$$

and

$$\frac{\partial^2 \boldsymbol{\Phi}}{\partial \Delta\boldsymbol{\gamma}^2} = -\frac{\partial^2 \boldsymbol{g}}{\partial \Delta\boldsymbol{\gamma}^2}. \tag{50}$$

Inserting Eqs. (42), (43), (48), (49) and (50) into Eq. (39) yields the final system of equations to be solved as

$$\begin{aligned} &\begin{bmatrix} 2\underline{\boldsymbol{P}}^T \underline{\mathbb{C}}^{\text{e}} \underline{\boldsymbol{P}} - \boldsymbol{H}(\boldsymbol{\gamma}) - \frac{\partial^2 \boldsymbol{g}}{\partial \Delta\gamma^2}\lambda - \Theta_\gamma \Delta\Gamma^{-1} & -\underline{\boldsymbol{P}}^T \underline{\mathbb{C}}^{\text{e}} \underline{\boldsymbol{P}} - \frac{\partial \boldsymbol{g}}{\partial \Delta\gamma}^T \\ \left(-\underline{\boldsymbol{P}}^T \underline{\mathbb{C}}^{\text{e}} \underline{\boldsymbol{P}} - \frac{\partial \boldsymbol{g}}{\partial \Delta\gamma}^T\right)^T & -\Lambda^{-1} S \end{bmatrix} \begin{bmatrix} \Delta\Delta\boldsymbol{\gamma} \\ \Delta\lambda \end{bmatrix} \\ &= \begin{bmatrix} \underline{\boldsymbol{P}}^T \underline{\mathbb{C}}^{\text{e}} \underline{\boldsymbol{\varepsilon}}^{\text{e,trial}} - 2\underline{\boldsymbol{P}}^T \underline{\mathbb{C}}^{\text{e}} \underline{\boldsymbol{P}} \Delta\boldsymbol{\gamma} + \boldsymbol{h}(\Delta\boldsymbol{\gamma}) + \left[\underline{\boldsymbol{P}}^{\text{T}} \underline{\mathbb{C}}^{\text{e}} \underline{\boldsymbol{P}} + \frac{\partial \boldsymbol{g}}{\partial \Delta\gamma}\right]\lambda + \mu\Delta\Gamma^{-1} e_m \\ -\underline{\boldsymbol{P}}^T \underline{\mathbb{C}}^{\text{e}}\left[\underline{\boldsymbol{\varepsilon}}^{\text{e,trial}} - \underline{\boldsymbol{P}}\Delta\boldsymbol{\gamma}\right] + \boldsymbol{g} - \mu\Lambda^{-1} e_m \end{bmatrix} \end{aligned} \tag{51}$$

with $\Delta\boldsymbol{\Gamma} = \text{diag}(\Delta\boldsymbol{\gamma}) \in \mathbb{R}^{m \times m}$ and the reformulation using the Lagrange multiplier $\boldsymbol{\rho}_\gamma$ where $\boldsymbol{\Theta}_\gamma = \text{diag}\left(\boldsymbol{\rho}_\gamma\right) \in \mathbb{R}^{m \times m}$ based on Eq. (39), see also Appendix A.2. The increment of the slack variable is given by

$$\Delta\boldsymbol{s} = -\Lambda^{-1} S \Delta\lambda - \boldsymbol{s} + \mu\Lambda^{-1} e_m \tag{52}$$

and the increment of the Lagrange multiplier to $\boldsymbol{\gamma}$, following Eq. (38) is defined by

$$\Delta\boldsymbol{\rho}_\gamma = \mu\Delta\Gamma^{-1} e_m - \Theta_\gamma \Delta\Gamma^{-1} \Delta\Delta\boldsymbol{\gamma} - \boldsymbol{\rho}_\gamma. \tag{53}$$

Comparing with the classical Kuhn-Tucker conditions from the Lagrangian function, see Eq. (20.3), we obtain $\lambda_i \Phi_i = 0 \; \forall i = 1, m$. These conditions replace the Kuhn-Tucker conditions from the problem definition of plasticity theory, see Eq. (6.3), which result as $\Phi_i \Delta\gamma_i = 0$ in the discretized form. During the solution, the condition $\lambda_i \Phi_i = 0$ is more simple to fulfill, since there is no direct dependency of Φ_i and λ_i. The constraint condition $\Delta\gamma_i \geqslant 0$ is ensured by the barrier function.

In a classical Newton algorithm, the update of the variables is done by

$$\Delta\boldsymbol{\gamma} \leftarrow \Delta\boldsymbol{\gamma} + \Delta\Delta\boldsymbol{\gamma}, \quad \lambda \leftarrow \lambda + \Delta\lambda, \quad \boldsymbol{s} \leftarrow \boldsymbol{s} + \Delta\boldsymbol{s}, \quad \boldsymbol{\rho}_\gamma \leftarrow \boldsymbol{\rho}_\gamma + \Delta\boldsymbol{\rho}_\gamma \tag{54}$$

until convergence is obtained related to the residual of the full system, compare Eq. (26), given by

$$\boldsymbol{r} = \begin{bmatrix} \underline{\boldsymbol{P}}^T \underline{\mathbb{C}}^{\mathrm{e}} \underline{\boldsymbol{\varepsilon}}^{\mathrm{e,trial}} - 2\underline{\boldsymbol{P}}^T \underline{\mathbb{C}}^{\mathrm{e}} \underline{\boldsymbol{P}} \Delta\boldsymbol{\gamma} + \boldsymbol{h}(\Delta\boldsymbol{\gamma}) + \left[\underline{\boldsymbol{P}}^{\mathrm{T}} \underline{\mathbb{C}}^{\mathrm{e}} \underline{\boldsymbol{P}} + \frac{\partial \boldsymbol{g}}{\partial \Delta\boldsymbol{\gamma}}\right] \boldsymbol{\lambda} + \mu \Delta\boldsymbol{\Gamma}^{-1} \boldsymbol{e}_m \\ -\underline{\boldsymbol{P}}^T \underline{\mathbb{C}}^{\mathrm{e}} \left[\underline{\boldsymbol{\varepsilon}}^{\mathrm{e,trial}} - \underline{\boldsymbol{P}} \Delta\boldsymbol{\gamma}\right] + \boldsymbol{g} - \boldsymbol{s} \\ -\boldsymbol{S}\boldsymbol{\lambda} + \mu \boldsymbol{e}_m \end{bmatrix}. \tag{55}$$

The first and second derivatives of the incremental slip resistance, $\frac{\partial \boldsymbol{g}}{\partial \Delta\boldsymbol{\gamma}}$ and $\frac{\partial^2 \boldsymbol{g}}{\partial \Delta\boldsymbol{\gamma}^2}$ are given by the hardening moduli $h^{\alpha\beta}$ and $h^{\alpha\beta\zeta}$, respectively,

$$h^{\alpha\beta} = \frac{\partial g^\alpha}{\partial \Delta\gamma^\beta} = \sum_\rho \left(\hat{h}(A)\delta^{\rho\beta} + \hat{h}\prime(A)\Delta\gamma^\rho\right)(q + (1-q)\delta^{\alpha\rho}) \tag{56}$$

and

$$\begin{aligned} h^{\alpha\beta\zeta} &= \frac{\partial^2 g^\alpha}{\partial \Delta\gamma^\beta \partial \Delta\gamma^\zeta} \\ &= \sum_\rho \left(\hat{h}\prime(A)\delta^{\rho\beta} + \hat{h}\prime\prime(A)\Delta\gamma^\rho + \hat{h}\prime(A)\delta^{\rho\zeta}\right)(q + (1-q)\delta^{\alpha\rho}) \end{aligned} \tag{57}$$

where $\alpha = 1,\dots,m, \beta = 1,\dots,m, \rho = 1,\dots,m$ and $\zeta = 1,\dots,m$. Here, the first and second derivative of the scalar function $\hat{h}(A)$ with respect to the increment of plastic slip is defined by $\hat{h}\prime(A)$ and $\hat{h}\prime\prime(A)$, respectively. Finally, the Schur complement of the matrix of the reduced system given in Eq. (51), as described in Scheunemann et al. (2020), is used to solve the system of equations efficiently.

4.1. Algorithmic consistent material tangent moduli

In addition to the determination of the plastic slip γ_{n+1} and the stresses $\boldsymbol{\sigma}_{n+1}$, the material tangent moduli need to be computed. The consistent algorithmic tangent moduli, which relate the total stress increment to the total strain incremenent with

$$\Delta\boldsymbol{\sigma}_{n+1} = \mathbb{C}^{\mathrm{ep}} : \Delta\boldsymbol{\varepsilon}_{n+1} \qquad \text{with} \qquad \mathbb{C}^{\mathrm{ep}} = \frac{\partial \boldsymbol{\sigma}_{n+1}}{\partial \boldsymbol{\varepsilon}_{n+1}}. \tag{58}$$

can be derived for the here presented approach through a reformulation of the stress increment as

$$\begin{aligned} \boldsymbol{\sigma}_{n+1} &= \mathbb{C}^{\mathrm{e}} : \boldsymbol{\varepsilon}^{\mathrm{e}}_{n+1} = \mathbb{C}^{\mathrm{e}} : \left[\boldsymbol{\varepsilon}_{n+1} - \boldsymbol{\varepsilon}^{\mathrm{p}}_{n+1}\right] = \mathbb{C}^{\mathrm{e}} : \left[\boldsymbol{\varepsilon}_{n+1} - \boldsymbol{\varepsilon}^{\mathrm{p}}_{n} - \Delta\boldsymbol{\varepsilon}^{\mathrm{p}}_{n+1}\right] \\ &= \mathbb{C}^{\mathrm{e}} : \left[\boldsymbol{\varepsilon}^{\mathrm{trial}}_{n+1} - \Delta\boldsymbol{\varepsilon}^{\mathrm{p}}_{n+1}\right] \\ &= \mathbb{C}^{\mathrm{e}} : \boldsymbol{\varepsilon}^{\mathrm{trial}}_{n+1} - \mathbb{C}^{\mathrm{e}} : \sum_\beta \Delta\gamma^\beta_{n+1} \boldsymbol{P}^\beta \end{aligned} \tag{59}$$

which leads to the consistent tangent moduli depending on the derivative of the slip increment with respect to the total strains by

$$\mathbb{C}^{\mathrm{ep}} = \mathbb{C}^{\mathrm{e}} - \sum_\beta \mathbb{C}^{\mathrm{e}} : \boldsymbol{P}^\beta \otimes \frac{\partial \Delta\gamma^\beta_{n+1}}{\partial \boldsymbol{\varepsilon}_{n+1}}. \tag{60}$$

Independently of the applied algorithm, this relation holds. The formulation of the algorithm which is used to determine the slip increments $\Delta\gamma^\alpha$ then yields the derivative $\frac{\partial \Delta\gamma^\beta_{n+1}}{\partial \boldsymbol{\varepsilon}_{n+1}}$, which here needs to be derived from the formulation of the IPDIPM. As noted in Scheunemann et al. (2020), the arising equation system at the material point level can be solved using a Schur complement in two different ways. The detailed derivation of the algorithmic consistent tangent moduli for both Schur complement formulations can be found in the Appendix A.1. Formulation 1 computes the derivative as

$$\begin{aligned} \frac{\partial \Delta\boldsymbol{\gamma}_{n+1}}{\partial \boldsymbol{\varepsilon}_{n+1}} &= \left[\boldsymbol{H}_{11} - \boldsymbol{H}_{12}\boldsymbol{H}_{22}^{-1}\boldsymbol{H}_{21}\right]^{-1} \left[-\underline{\boldsymbol{P}}\underline{\mathbb{C}}^{\mathrm{e}} + \boldsymbol{H}_{12}\boldsymbol{H}_{22}^{-1}\underline{\boldsymbol{P}}\underline{\mathbb{C}}^{\mathrm{e}}\right] \\ &= \left[\boldsymbol{H}_{11} - \boldsymbol{H}_{12}\boldsymbol{H}_{22}^{-1}\boldsymbol{H}_{21}\right]^{-1} \left[-\boldsymbol{I} + \boldsymbol{H}_{12}\boldsymbol{H}_{22}^{-1}\right]\underline{\boldsymbol{P}}\underline{\mathbb{C}}^{\mathrm{e}} \\ &= \left(-\left[\boldsymbol{H}_{11} - \boldsymbol{H}_{12}\boldsymbol{H}_{22}^{-1}\boldsymbol{H}_{21}\right]^{-1} + \left[\boldsymbol{H}_{11} - \boldsymbol{H}_{12}\boldsymbol{H}_{22}^{-1}\boldsymbol{H}_{21}\right]^{-1}\left[\boldsymbol{H}_{12}\boldsymbol{H}_{22}^{-1}\right]\right)\underline{\boldsymbol{P}}\underline{\mathbb{C}}^{\mathrm{e}} \\ &= \boldsymbol{C}_{\mathrm{fact}}\underline{\boldsymbol{P}}\underline{\mathbb{C}}^{\mathrm{e}} \end{aligned} \tag{61}$$

with

$$\begin{aligned} \boldsymbol{H}_{11} &= -\frac{\partial^2 D}{\partial \Delta\boldsymbol{\gamma}^2} + \frac{\partial^2 \boldsymbol{\Phi}}{\partial \Delta\boldsymbol{\gamma}^2}\boldsymbol{\lambda} + \mu\boldsymbol{\Gamma}^{-2} \\ &= 2\underline{\boldsymbol{P}}^T\underline{\mathbb{C}}^{\mathrm{e}}\underline{\boldsymbol{P}} - \frac{\partial^2 \Delta\boldsymbol{g}}{\partial \Delta\boldsymbol{\gamma}^2}\Delta\boldsymbol{\gamma} - 2\frac{\partial \Delta\boldsymbol{g}}{\partial \Delta\boldsymbol{\gamma}} - \frac{\partial^2 \Delta\boldsymbol{g}}{\partial \Delta\boldsymbol{\gamma}^2}\boldsymbol{\lambda} + \mu\boldsymbol{\Gamma}^{-2} \\ \boldsymbol{H}_{12} &= \frac{\partial \boldsymbol{\Phi}^T}{\partial \Delta\boldsymbol{\gamma}} = -\underline{\boldsymbol{P}}\underline{\mathbb{C}}^{\mathrm{e}}\underline{\boldsymbol{P}}^T - \frac{\partial \Delta\boldsymbol{g}^T}{\partial \Delta\boldsymbol{\gamma}} \\ \boldsymbol{H}_{21} &= \frac{\partial \boldsymbol{\Phi}}{\partial \Delta\boldsymbol{\gamma}} = -\underline{\boldsymbol{P}}^T\underline{\mathbb{C}}^{\mathrm{e}}\underline{\boldsymbol{P}} - \frac{\partial \Delta\boldsymbol{g}}{\partial \Delta\boldsymbol{\gamma}} \\ \boldsymbol{H}_{22} &= -\boldsymbol{\Lambda}^{-1}\boldsymbol{S} \end{aligned} \tag{62}$$

which leads to the final statement for the tangent moduli in Voigt notation

$$\underline{\mathbb{C}}^{\mathrm{ep}} = \underline{\mathbb{C}}^{\mathrm{e}} - \underline{\mathbb{C}}^{\mathrm{e}}\,\underline{\boldsymbol{P}}^T\boldsymbol{C}_{\mathrm{fact}}\underline{\boldsymbol{P}}\,\underline{\mathbb{C}}^{\mathrm{e}}. \tag{63}$$

The second formulation of the Schur complement first computes the increment of the Lagrange multiplier λ and finally results in

$$\frac{\partial \Delta\boldsymbol{\gamma}_{n+1}}{\partial \boldsymbol{\varepsilon}_{n+1}} = (\overline{\boldsymbol{H}}_2 - \overline{\boldsymbol{H}}_1)\underline{\boldsymbol{P}}\underline{\mathbb{C}}^{\mathrm{e}} = \boldsymbol{C}_{\mathrm{fact}}\underline{\boldsymbol{P}}\,\underline{\mathbb{C}}^{\mathrm{e}} \tag{64}$$

with

$$\overline{\boldsymbol{H}}_1 = \left(\boldsymbol{H}_{11}^{-1} + \boldsymbol{H}_{11}^{-1}\boldsymbol{H}_{12}\left[\boldsymbol{H}_{22} - \boldsymbol{H}_{21}\boldsymbol{H}_{11}^{-1}\boldsymbol{H}_{12}\right]^{-1}\boldsymbol{H}_{21}\boldsymbol{H}_{11}^{-1}\right) \tag{65}$$

and

$$\overline{\boldsymbol{H}}_2 = \left(\boldsymbol{H}_{11}^{-1}\boldsymbol{H}_{12}\left[\boldsymbol{H}_{22} - \boldsymbol{H}_{21}\boldsymbol{H}_{11}^{-1}\boldsymbol{H}_{12}\right]^{-1}\right) \tag{66}$$

and the resulting tangent moduli arise as according to Eq. (58) and (63), in Voigt notation, respectively. The related algorithm for the computation of $\mathbb{C}^{\mathrm{ep}}_{\mathrm{algo}}$ in a finite element framework is shown in Algorithm 1.

Algorithm 1: Computation of algorithmic consistent material tangent

1: **Procedure** On material point level
2: Solve local stress update algorithm based on the IPDIPM
3: Compute material tangent:

$$\underline{\mathbb{C}}^{\mathrm{ep}}_{\mathrm{algo}} = \underline{\mathbb{C}}^{\mathrm{e}} - \underline{\mathbb{C}}^{\mathrm{e}}\,\underline{\boldsymbol{P}}^T\boldsymbol{C}_{\mathrm{fact}}\underline{\boldsymbol{P}}\,\underline{\mathbb{C}}^{\mathrm{e}} \tag{67}$$

4: with $\boldsymbol{C}_{\mathrm{fact}}$ according to Eq. (61) or (64)
5: **end procedure**

4.2. Numerical approximation of material tangent moduli and element stiffness matrix

Beside the algorithmic consistent tangent, there exists the framework of perturbation analysis based on a finite difference scheme to compute the material tangent, where an alternative version to the classical perturbation of the real space is provided by the complex step derivative approximation, see e.g. Tanaka et al. (2014), among others. Numerical approximation schemes for tangent moduli can be obtained from finite difference (FD) schemes, which are however governed by a well known sensitivity with

respect to the perturbation, especially in highly nonlinear problems due to round off errors in floating point arithmetics. A way to overcome such problems in numerical approximation schemes was proposed by Lyness (1968) by the complex-step derivative approximation (CSDA) scheme for scalar valued derivatives of first order. The scheme uses perturbation along the imaginary axis of complex numbers and thus avoids the direct addition of perturbations along the same axis, which is the cause of round off errors in FD schemes. Lai and Crassidis (2008) extended the scheme to higher order scalar valued numerical derivatives. Applications of the CSDA scheme to computational plasticity are shown in Pérez-Foguet et al. (2000a,b), Tanaka et al. (2014) use the robust scheme for the derivation of tangent moduli and localization analysis, tangent moduli at finite strains were also discussed and derived in Sun et al. (2008). The computation of the stiffness matrix in a finite element problem based on a CSDA scheme is described in Kim et al. (2011).

The CSDA technique uses a Taylor series expansion of a scalar valued function $f(x)$ along the imaginary axis, i.e.,

$$f(x+\mathrm{i}h) = f(x) + \mathrm{i}hf'(x) - \frac{h^2}{2!}f''(x) - \mathrm{i}\frac{h^3}{3!}f'''(x) + \dots \tag{68}$$

where $\mathrm{i}^2 = -1$ is the imaginary unit. The derivative $f'(x)$ is obtained considering only the parts along the imaginary axis yielding

$$\mathscr{I}[f(x+\mathrm{i}h)] = hf'(x) + \mathscr{O}\left(h^3\right) \tag{69}$$

which leads to the approximation

$$f'(x) \approx \frac{\mathscr{I}[f(x+\mathrm{i}h)]}{h}, \tag{70}$$

neglecting higher order terms. Since no subtraction operation is included in the operations of Eq. (70), round off errors can never occur. For higher order functions, following Tanaka et al. (2014), the CSDA scheme extends to directional derivatives of tensor fields with $\boldsymbol{A}$ defining an arbitrary tensor on $\mathbb{R}^{2\times2}$ or $\mathbb{R}^{3\times3}$. Then the directional derivative of a tensorial function $\boldsymbol{Y}(\boldsymbol{X})$ of a tensor argument $\boldsymbol{X}$ in the direction $\boldsymbol{A}$ is given by

$$\mathrm{D}\boldsymbol{Y}(\boldsymbol{X})[\boldsymbol{A}] := \lim_{h\to0}\frac{\boldsymbol{Y}(\boldsymbol{X}+h\boldsymbol{A}) - \boldsymbol{Y}(\boldsymbol{X})}{h} = \frac{\partial \boldsymbol{Y}}{\partial \boldsymbol{X}} : \boldsymbol{A}. \tag{71}$$

where $\frac{\partial \boldsymbol{Y}}{\partial \boldsymbol{X}}$ is a second-order tensor describing the gradient of $\boldsymbol{Y}$ with respect to $\boldsymbol{X}$. Using the CSDA scheme, this approximation of the argument leads to

$$\frac{\partial \boldsymbol{Y}}{\partial \boldsymbol{X}} : \boldsymbol{A} \approx \frac{\mathscr{I}[\boldsymbol{Y}(\boldsymbol{X}+\mathrm{i}h\boldsymbol{A})]}{h}. \tag{72}$$

For the application to the present case, the material tangent moduli $\mathbb{C}^{\mathrm{ep}}$ will be approximated using the CSDA scheme to compute $\mathbb{C}^{\mathrm{ep}}_{\mathrm{CSDA}}$. Therefore, based on Eq. (58), we substitute $\boldsymbol{\sigma}$ in $\boldsymbol{Y}, \boldsymbol{\varepsilon}$ in $\boldsymbol{X}$ and consider $\overset{\star}{\boldsymbol{\varepsilon}}{}^{ij} = \boldsymbol{e}^i \otimes \boldsymbol{e}^j$ and thereby consider the approximation of the derivative in the cartesian base. This reformulates Eq. (72) to

$$\mathbb{C}^{\mathrm{ep}}_{\mathrm{CSDA}} : \overset{\star}{\boldsymbol{\varepsilon}} = \frac{\mathscr{I}\left[\boldsymbol{\sigma}\left(\boldsymbol{\varepsilon} + \mathrm{i}h\overset{\star}{\boldsymbol{\varepsilon}}\right)\right]}{h}. \tag{73}$$

The algorithmic realization of the computation of the approximation of the material tangent is given in detail in Algorithm 2.

Algorithm 2: Computation of material tangent using CSDA scheme

1: **Procedure** Perturbation on material point level
2: loop perturbation: $(K) = 1\dots3, (L) = 1\dots3$
3: Calculate $\overset{\star}{\boldsymbol{\varepsilon}} = \boldsymbol{e}^{(K)} \otimes \boldsymbol{e}^{(L)}$
4: Calculate stress response: $\boldsymbol{\sigma}\left(\boldsymbol{\varepsilon} + \mathrm{i}h\overset{\star}{\boldsymbol{\varepsilon}}\right)$
5: by based on stress update algorithm using IPDIPM
6: Evaluate material tangent:

$$\mathbb{C}^{\mathrm{ep}IJ(K)(L)}_{\mathrm{CSDA}} = \frac{\mathscr{I}\left[\sigma^{IJ}\left(\boldsymbol{\varepsilon} + \mathrm{i}h\overset{\star}{\boldsymbol{\varepsilon}}\right)\right]}{h} \tag{74}$$

7: end loop perturbation
8: Evaluate undisturbed stress response: $\boldsymbol{\sigma}(\boldsymbol{\varepsilon})$
9: end procedure

In the finite element formulation, the consistent tangent moduli are required for the application of a Newton–Raphson scheme on the global system of equations. Without explicitly computing the material tangent moduli, another approximation scheme is possible. Following the work of Kim et al. (2011), the CSDA scheme can be applied to derive the finite element stiffness matrices by differentiating the internal force vector with respect to the displacement vector. In this work, this idea is used to compute the approximation of the element stiffness matrix $\boldsymbol{k}^{\mathrm{e}}_{\mathrm{CSDA}}$, the according algorithm is given in Algorithm 3. The element vector of nodal displacement is clasically defined as

$$\boldsymbol{d}^{\mathrm{e}} = \left[d^{\mathrm{e}}_1\ d^{\mathrm{e}}_2 \dots d^{\mathrm{e}}_{\mathrm{tdof}}\right]^{\mathrm{T}} \tag{75}$$

with tdof = nen × ndf and the element force vector is defined by

$$\boldsymbol{p}^{\mathrm{e}} = \left[p^{\mathrm{e}}_1\ p^{\mathrm{e}}_2 \dots p^{\mathrm{e}}_{\mathrm{tdof}}\right]^{\mathrm{T}} \tag{76}$$

Then, the element stiffness matrix is obtained based on

$$\boldsymbol{k}^{\mathrm{e}} = \left[\frac{\partial \boldsymbol{p}^{\mathrm{e}}}{\partial d^{\mathrm{e}}_1} \mid \frac{\partial \boldsymbol{p}^{\mathrm{e}}}{\partial d^{\mathrm{e}}_2} \mid \dots \mid \frac{\partial \boldsymbol{p}^{\mathrm{e}}}{\partial d^{\mathrm{e}}_{\mathrm{tdof}}}\right]. \tag{77}$$

Algorithm 3: Computation of element stiffness matrix using CSDA scheme

1: **Procedure** Perturbation on finite element level 2: loop perturbation: $J = 1 \ldots \text{nen} \times \text{ndf}$
3: Determine perturbed version of $\boldsymbol{d}^{\mathrm{e}}$:
4: loop $K = 1 \ldots \text{tdof}$
5:

$$\overset{\sim}{\boldsymbol{d}}^{\mathrm{e}} \begin{cases} \tilde{d}{}^{\mathrm{e}}_K = d^{\mathrm{e}}_K + \mathrm{i}h & \text{if } K == J \\ \tilde{d}{}^{\mathrm{e}}_K = d^{\mathrm{e}}_K & \text{else} \end{cases} \tag{78}$$

6: end loop
7: loop for all Gauss points:
8: Compute $\tilde{\boldsymbol{p}}^{\mathrm{e}}\left(\tilde{\boldsymbol{d}}^{\mathrm{e}}\right)$ based on perturbed displacement vector
9: solving stress update algorithm based on IPDIPM
10: Compute column J of element stiffness matrix:
11:

$$k^{\mathrm{e}}(I,J) = \sum_{\mathrm{GP}} \frac{\mathcal{I}[\tilde{p}^{\mathrm{e}}(I)]}{h} \tag{79}$$

12: end loop Gauss
13: end loop perturbation
14: Evaluate undisturbed element force vector $\boldsymbol{p}^{\mathrm{e}}(\boldsymbol{d}^{\mathrm{e}})$
15: end procedure

5. Numerical examples

5.1. Study of an academic case: two perpendicular slip systems

As an academic example, a study of a crystal with two slip systems is performed in the following. This case is considered since it simplifies the formulation with less slip systems but still captures the property of linear dependent slip systems which is inherent to face-centered cubic crystals. The orientation of the slip systems is given by

$$\boldsymbol{s}_1 = \left[1/\sqrt{2} \quad 0 \quad 1/\sqrt{(2)}\right]^{\mathrm{T}} \quad \boldsymbol{n}_1 = \left[-1/\sqrt{2} \quad 0 \quad 1/\sqrt{(2)}\right]^{\mathrm{T}}, \tag{80}$$

$$\boldsymbol{s}_2 = \left[-1/\sqrt{2} \quad 0 \quad 1/\sqrt{(2)}\right]^{\mathrm{T}} \quad \boldsymbol{n}_2 = \left[1/\sqrt{2} \quad 0 \quad 1/\sqrt{(2)}\right]^{\mathrm{T}}. \tag{81}$$

A simulation of a homogeneous tension test in z-direction using one hexahedral finite element is carried out. Thereby, the direct comparison of the computed material tangent moduli from Algorithms 1 and 2 becomes possible. Algorithm 3 is not considered in the comparison, since it leads to the same result and convergence behavior as Algorithm 2, as it is also shown in Section 5.2. Furthermore, the comparison of Algorithm 3 with Algorithm 1 is only possible based on the element stiffness matrix, since the material tangent is not computed explicitly in Algorithm 3. Hence, in the comparison of Algorithms 1 and 2 for the material tangent moduli, only minor differences can be seen. The material tangent moduli for one Gauss point are shown exemplarily to illustrate these differences in Fig. 2.

The difference in the values which can be seen is in the range 10^3. In order to examine this further, the plastic correction part of the tangent moduli is considered, which can be described as $\underline{\mathbb{C}}^{\mathrm{plas}}_{\mathrm{CSDA}} = \underline{\mathbb{C}}^{\mathrm{ep}} - \underline{\mathbb{C}}^{\mathrm{e}}$ for Algorithm 2 or directly by $\underline{\mathbb{C}}^{\mathrm{plas}}_{\mathrm{algo}} = \underline{\mathbb{C}}^{e}\underline{\boldsymbol{P}}^{T}\boldsymbol{C}_{\mathrm{fact}}\underline{\boldsymbol{P}}\,\underline{\mathbb{C}}^{\mathrm{e}}$ for Algorithm 1. For the tangent moduli given in Fig. 2, these are shown in Fig. 3.

The entries of $\underline{\mathbb{C}}^{\mathrm{plas}}_{\mathrm{algo}}$ and $\underline{\mathbb{C}}^{\mathrm{plas}}_{\mathrm{CSDA}}$ are in the range of 10^4. It should be noted that in the case of Algorithm 1, for the computation of the plastic corrector part, values in $\boldsymbol{C}_{\mathrm{fact}}$ which are in the range of 10^{-3}, are multiplied with the remaining terms, which are in the order of 10^9, and a summation of the products is carried out. Thus, a difference in an entry in $\boldsymbol{C}_{\mathrm{fact}}$ in the second decimal place, i.e. 10^{-5}, will result in a change in the tangent moduli in the range 10^4. Due to the fact that $\boldsymbol{C}_{\mathrm{fact}}$ requires several matrix inversions of submatrices of the Hessian of the Interior Point problem, which are not necessarily well-conditioned, such deficiencies of $\boldsymbol{C}_{\mathrm{fact}}$ may occur and are assumed to be the root of the difference in the differences in the tangent moduli in addition to possible round-off errors occuring during the summation. Additionally, a nonsymmetric representation of $\underline{\mathbb{C}}^{\mathrm{plas}}_{\mathrm{CSDA}}$ can be seen which cannot be described by the algorithmic counterpart by definition.

The convergency of the norm of the residual for different time steps is shown in Fig. 4. Quadratic convergence can be seen for both algorithms. The norm of the increments of displacement are in the range of 10^{-12} to 10^{-13} for Algorithm 1 and between 10^{-13} and 10^{-18} for Algorithm 2.

Regarding the information from the local algorithm solved using the interior point method, a major difference is that Algorithm 1 needs the information of the Hessian matrix, whereas Algorithm 2 uses the result $\Delta\boldsymbol{\gamma}$ through its relation to the stress $\boldsymbol{\sigma}$. For the computation of the tangent moduli in Algorithm 1, the computation of the inverse within the Schur complement is necessary. The invertibility of the matrices have been checked through the deviation of the matrix product with its inverse from the identity. The norm of this matrix product did not exceed the value of 10^{-10}, leading to the assumption that the inverse is computed appropriately. Regarding the eigenvalues, for the Hessian the requirement is that the number of positive and negative eigenval-

$$\underline{\mathbb{C}}^{\mathrm{ep}}_{\mathrm{algo}} = \begin{bmatrix} 25.7975E+04 & 17.8025E+04 & 25.0667E+04 & 0.00000E+00 & 0.00000E+00 & 0.00000E+00 \\ 17.8025E+04 & 33.0617E+04 & 17.8025E+04 & 0.00000E+00 & 0.00000E+00 & 0.00000E+00 \\ 25.0667E+04 & 17.8025E+04 & 25.7975E+04 & 0.00000E+00 & 0.00000E+00 & 0.00000E+00 \\ 0.00000E+00 & 0.00000E+00 & 0.00000E+00 & 76.2963E+03 & 0.00000E+00 & 0.00000E+00 \\ 0.00000E+00 & 0.00000E+00 & 0.00000E+00 & 0.00000E+00 & 76.2963E+03 & 0.00000E+00 \\ 0.00000E+00 & 0.00000E+00 & 0.00000E+00 & 0.00000E+00 & 0.00000E+00 & 76.2963E+03 \end{bmatrix},$$

$$\underline{\mathbb{C}}^{\mathrm{ep}}_{\mathrm{CSDA}} = \begin{bmatrix} 25.5552E+04 & 17.8025E+04 & 25.3090E+04 & 0.00000E+00 & 0.00000E+00 & 0.00000E+00 \\ 17.8025E+04 & 33.0617E+04 & 17.8025E+04 & 0.00000E+00 & 0.00000E+00 & 0.00000E+00 \\ 25.3090E+04 & 17.8025E+04 & 25.5552E+04 & 0.00000E+00 & 0.00000E+00 & 0.00000E+00 \\ 0.00000E+00 & 0.00000E+00 & 0.00000E+00 & 76.2963E+03 & 0.00000E+00 & 0.00000E+00 \\ 0.00000E+00 & 0.00000E+00 & 0.00000E+00 & 0.00000E+00 & 76.2963E+03 & 0.00000E+00 \\ 0.00000E+00 & 0.00000E+00 & 0.00000E+00 & 0.00000E+00 & 0.00000E+00 & 76.2963E+03 \end{bmatrix}$$

Fig. 2. Tangent moduli from simple tension test: Gauss point 10, t = 0.1, first iteration.

$$\underline{\mathbb{C}}^{\text{plas}}_{\text{algo}} = \begin{bmatrix} 72.6421E+03 & 0.00000E+00 & -72.6421E+03 & 0.00000E+00 & 0.00000E+00 & 0.00000E+00 \\ 0.00000E+00 & 0.00000E+00 & 0.00000E+00 & 0.00000E+00 & 0.00000E+00 & 0.00000E+00 \\ -72.6421E+03 & 0.00000E+00 & 72.6421E+03 & 0.00000E+00 & 0.00000E+00 & 0.00000E+00 \\ 0.00000E+00 & 0.00000E+00 & 0.00000E+00 & 0.00000E+00 & 0.00000E+00 & 0.00000E+00 \\ 0.00000E+00 & 0.00000E+00 & 0.00000E+00 & 0.00000E+00 & 0.00000E+00 & 0.00000E+00 \\ 0.00000E+00 & 0.00000E+00 & 0.00000E+00 & 0.00000E+00 & 0.00000E+00 & 0.00000E+00 \end{bmatrix},$$

$$\underline{\mathbb{C}}^{\text{plas}}_{\text{CSDA}} = \begin{bmatrix} 75.0650E+03 & 0.00000E+00 & -75.0650E+03 & 0.00000E+00 & 0.00000E+00 & 0.00000E+00 \\ 29.1038E-12 & 58.2077E-12 & 29.1038E-12 & 0.00000E+00 & 0.00000E+00 & 0.00000E+00 \\ -75.0650E+03 & 0.00000E+00 & 75.0650E+03 & 0.00000E+00 & 0.00000E+00 & 0.00000E+00 \\ 0.00000E+00 & 0.00000E+00 & 0.00000E+00 & 0.00000E+00 & 0.00000E+00 & 0.00000E+00 \\ 0.00000E+00 & 0.00000E+00 & 0.00000E+00 & 0.00000E+00 & 0.00000E+00 & 0.00000E+00 \\ 0.00000E+00 & 0.00000E+00 & 0.00000E+00 & 0.00000E+00 & 0.00000E+00 & 0.00000E+00 \end{bmatrix}.$$

Fig. 3. $\underline{\mathbb{C}}^{\text{plas}}_{\text{algo}}$ and $\underline{\mathbb{C}}^{\text{plas}}_{\text{CSDA}}$ from simple tension test: Gauss point 10, t = 0.1, first iteration.

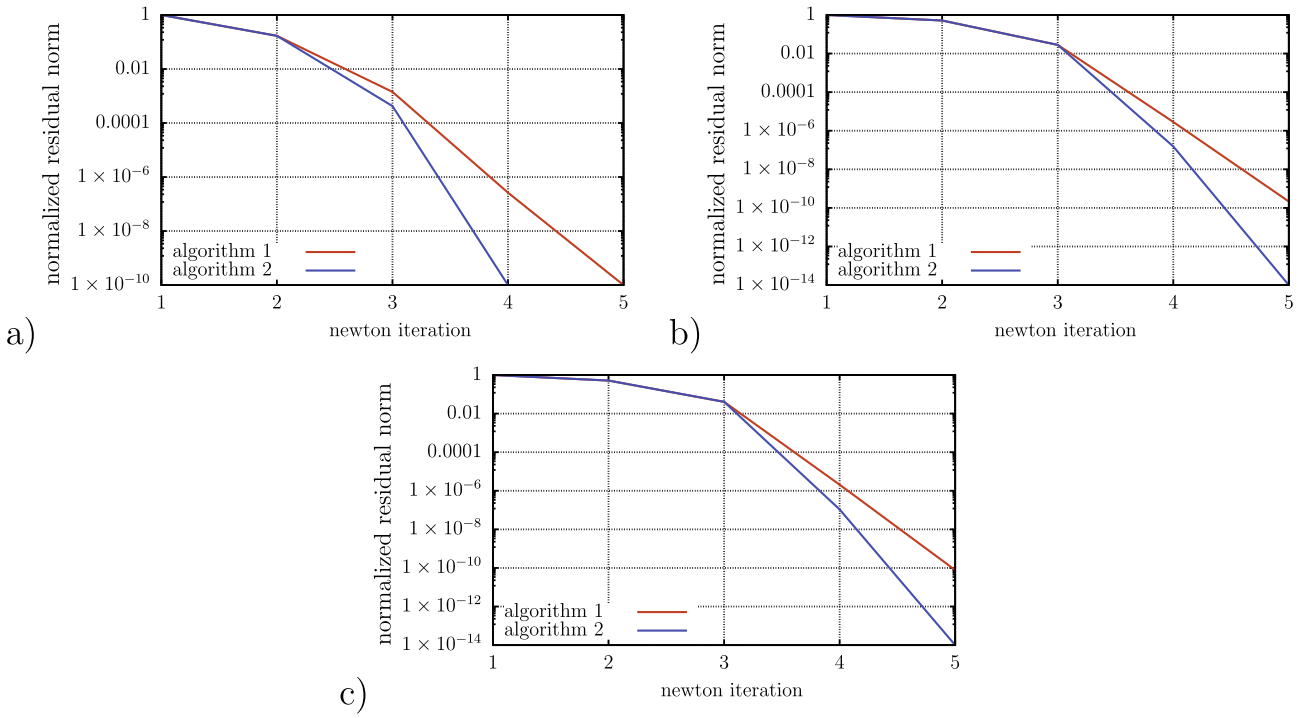

Fig. 4. Convergency of normalized residual of Algorithms 1 and 2 for (a) t = 0.01, (b) t = 0.05 and (c) t = 0.1.

ues is identical in order not to loose the curvature of the problem, which was also not violated. The condition number of the $\boldsymbol{H}_{11}$ and the Schur complement, see Appendix A.1, which need to be inverted range between 10^3 and 10^6 and 10^2 and 10^6, respectively. The slip computed at the Gauss point as well as the resulting stresses are identical, i.e.

$$\underline{\boldsymbol{\sigma}} = \begin{bmatrix} -27.8657E-01 \\ 17.7636E-16 \\ 17.2117E+00 \\ -51.7004E-17 \\ -53.4541E-02 \\ 16.2669E-17 \end{bmatrix} \quad \boldsymbol{\gamma} = \begin{bmatrix} 11.7135E-06 \\ 11.7135E-06 \end{bmatrix} \tag{82}$$

and especially the result for $\boldsymbol{\gamma}$ is in accordance with the theoretical result of identical slip on both systems.

5.2. Uniaxial extension of solid with varying monocrystal orientations

Following Borja and Rahmani (2012), a displacement driven uniaxial deformation of a cubic solid in 3D is considered. The cubic solid measures 1 m×1 m×3 m and is meshed with 3×3×8 27-noded hexahedral finite elements. On the bottom surface, the displacement in all directions is restricted whereas on the top surface, a vertical displacement of $\delta(t)$ with a final displacement of $\delta = 0.03$ m is applied. The displacement in x- and y-direction of the top surface is free. A monocrystal is considered with different orientations of the underlying crystalline structure with respect to the reference frame, given by the angles ϕ_1, ϕ_2 and ϕ_3 related to the rotation matrices

$$\boldsymbol{\Theta}_1 = \begin{bmatrix} \cos\phi_1 & \sin\phi_1 & 0 \\ -\sin\phi_1 & \cos\phi_1 & 0 \\ 0 & 0 & 1 \end{bmatrix}, \boldsymbol{\Theta}_2 = \begin{bmatrix} \cos\phi_2 & 0 & -\sin\phi_2 \\ 0 & 1 & 0 \\ \sin\phi_2 & 0 & \cos\phi_2 \end{bmatrix},$$
$$\boldsymbol{\Theta}_3 = \begin{bmatrix} \cos\phi_3 & \sin\phi_3 & 0 \\ -\sin\phi_3 & \cos\phi_3 & 0 \\ 0 & 0 & 1 \end{bmatrix} \tag{83}$$

describing the rotation $\boldsymbol{e}_i = \boldsymbol{R}\bar{\boldsymbol{e}}_i$ with $\boldsymbol{R} = \boldsymbol{\Theta}_3\boldsymbol{\Theta}_2\boldsymbol{\Theta}_1$ of the reference orthogonal axes $\{\bar{\boldsymbol{e}}_i\}_{i=1,3}$. The crystalline structure induces anisotropy which is why the cubic solid undergoes different deformations related to the orientation of the underlying crystalline

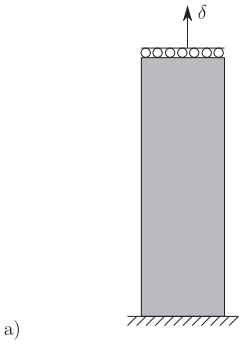

b)

Young's Module	15000 MPa
Poisson's ratio	0.37
yield strength	20 MPa

Fig. 5. Boundary value problem: Cubic solid with uniaxial extension in z-direction.

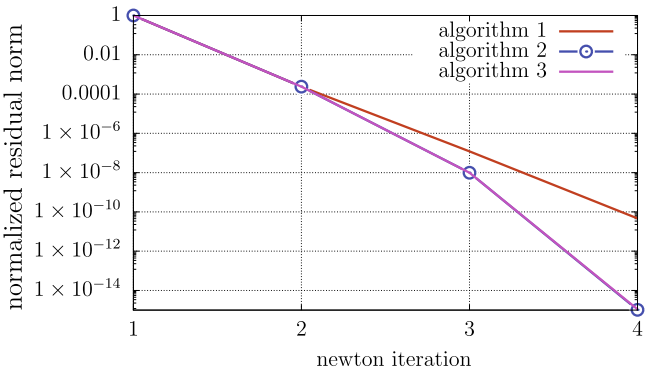

Fig. 6. Convergency of normalized residual of Algorithms 1–3 at $t = 0.3$.

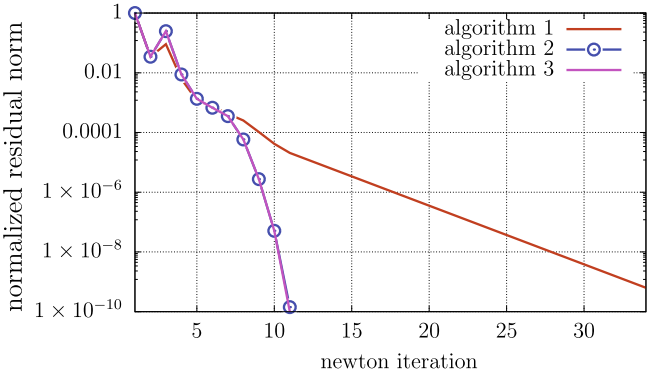

Fig. 7. Convergency of normalized residual of Algorithms 1–3 at $t = 0.4$.

structure. In the following, three orientation set ups will be considered: orientation 1 is described by $(\phi_1, \phi_2, \phi_3) = (0, 0, 0)$, orientation 2 uses $(\phi_1, \phi_2, \phi_3) = (0, 20, 0)$ and orientation 3 is defined by $(\phi_1, \phi_2, \phi_3) = (0, -20, 0)$. Fig. 5a illustrates the boundary value problem. An isotropic elastic behavior is considered with the material parameters given in Fig. 5b together with the initial yield strength which is equal on all slip systems. Ideal plastic behavior, thus no hardening was considered in the simulations. Note that in the presented algorithm, an update of the barrier parameter $\mu_{i+1} = 0.5\mu_i$ has been used within the interior point method with $\mu \to \mu_{\text{end}}$ and a final value of $\mu_{\text{end}} = 1 \times 10^{-8}$. The update scheme and the initial value have been chosen heuristically here. This choice has a strong incluence on the problem, however a detailed investigation is beyond the scope of this paper.

For orientation 1, the convergency of the global Newton–Raphson scheme based on the three algorithmic set ups described in Section A.1 and Section 4.2 is shown in Table 1 for pseudo time steps $t = 0.3$ and $t = 0.4$, a time increment of $\Delta t = 0.01$ is used here. The behavior is additionally illustrated in Fig. 6 and Fig. 7. For $t = 0.3$, approximately quadratic convergence can be seen for all three algorithms, where convergence is obtained after four iterations. For $t = 0.4$, it can be seen that the convergency in this problem does not show quadratic behavior in all three algorithms. The convergence behavior in the first seven steps is similar for all variants of the algorithm. Algorithms 2 and 3 are considered to have converged after 11 steps. The convergence of Algorithm 1 based on the analytical tangent is slower and reaches convergence after 34 iteration steps. This unexpected convergence behavior shows similarities to the analysis which has been presented in Section 5.1 for an academic crystal with two slip systems. It is interesting to notice that the convergency of all three algorithms behaves very similar in the first iteration steps. A detailed analysis of the matrix inversions required for the computation of $\boldsymbol{C}_{\text{fact}}$ as well as the eigenvalues and condition numbers, compare Section 5.1 did not show a different behavior as described there.

Note that even though the convergence of the algorithmic tangent formulation is slower compared to the other two, considering the computing time it is favorable, since it needs overall less evaluations of the local problem formulation. Due to the application of perturbations, the local algorithm computing the stress update needs to be evaluated multiple times. In detail, for Algorithm 2,

Table 1
Convergency of normalized residual norm in uniaxial extension of cubic solid.

prop	iteration	$\mathbb{C}^{\text{ep}}_{\text{analy}}$	$\mathbb{C}^{\text{ep}}_{\text{CSDA}}$	$\boldsymbol{K}_{\text{CSDA}}$
0.3	1	1.0000000E+00	1.0000000E+00	1.0000000E+00
	2	2.3851323E-04	2.3851323E-04	2.3851323E-04
	3	1.2060784E-07	9.8078069E-09	9.8078070E-09
	4	4.6834707E-11	1.0309639E-15	1.0982250E-15
	...			
0.4	1	1.0000000E+00	1.0000000E+00	1.0000000E+00
	2	3.4232050E-02	3.4328684E-02	3.4328684E-02
	3	9.0620214E-02	2.4683139E-01	2.4683139E-01
	4	6.1554008E-03	8.7893006E-03	8.7893006E-03
	5	1.1742573E-03	1.3359071E-03	1.3359071E-03
	6	7.4618707E-04	6.7237895E-04	6.7237895E-04
	7	4.2267664E-04	3.5406731E-04	3.5406728E-04
	8	2.5204991E-04	5.8460422E-05	5.8460408E-05
	9	1.0362501E-04	2.7472888E-06	2.7472916E-06
	10	4.1827178E-05	5.0937466E-08	5.1039305E-08
	11	2.0624644E-05	1.4181227E-10	8.1489217E-11
	...	...	-	-
	34	6.3138933E-10	-	-

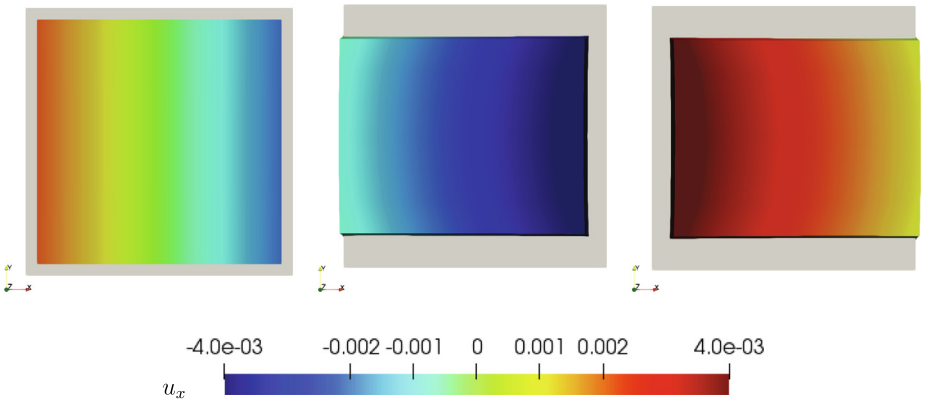

Fig. 8. Top view of displacement in *x*-direction on deformed solid. The initial shape of the solid is shown in grey: Orientation 1 (left), orientation 2 (middle), orientation 3 (right).

the local interior point algorithm needs to be evaluated seven times at each Gauss point, since the six entries of $\underline{\boldsymbol{\varepsilon}}$ need to be perturbed and one solution must be computed without any perturbation. For Algorithm 3, the number of perturbation loops is number of degrees of freedom plus an additional solution without any perturbation. This can also be seen from the loop counters in Algorithms 2 and 3. If the time required to solve the local problem at the material point level is low, this does not have a large impact of the computing time, however, in the case of the local algorithm used here, this has a major impact on the computing time. Therefore, in the comparison of the different orientations, Algorithm 1 based on the algorithmic tangent moduli $\mathbb{C}^{\text{ep}}_{\text{algo}}$ is used. The second formulation given in Appendix A.1 is used, however, both formulations lead to the same result and should be chosen in accordance with the chosen Schur complement to solve the local problem. Please note that the resulting activity of the slip does not depend on the chosen tangent moduli formulation.

A comparison of the different orientation set ups is done in the following. The anisotropy induced by the underlying crystalline structure leads to specific deformation pattern of the cubic solid. This is illustrated for all three considered orientations in Fig. 8 and Fig. 9, where the position of the initial shape of the top surface is shown in grey. The deformed shape of the cubic solid at pseudo time $t = 1$ can be seen with the displacement scaled by a factor of 20 in all illustrations. In Fig. 8, the coloring indicates the displacement in *x*-direction, Fig. 9 shows the displacement in *y*-direction.

For orientation 1, the applied displacement leads to an extension in *z*-direction and lateral contraction in *x*- and *y*-direction such that no predominant shearing in one direction is seen. This can be related to the equal activity on slip systems 1,2,4,5,7,8,10,12 in the homogeneous case. For orientation 2, from the consideration of a homogeneous problem, a shearing of the cubic solid with respect to ε_{13} whereas $\varepsilon_{23} \approx 0$ results, which agrees the results shown here. In this orientation in a homogeneous deformation state, the maximum Schmid stress and thus the dominant activated slip is found in slip system 4 and 10. This activity leads to a shearing of the cubic solid in positive *x*-direction, whereas the deformation in *y*-direction of the solid results from the lateral contraction. In orientation 3, from the consideration of a homogeneous deformation state, slip systems 1 and 7 are the dominant active systems and the deformation of the cubic solid into the opposite direction of orientation 2 can be seen with respect to the displacement in *x*-direction. Lateral contraction in *y*-direction is observed similarly to orientation 2.

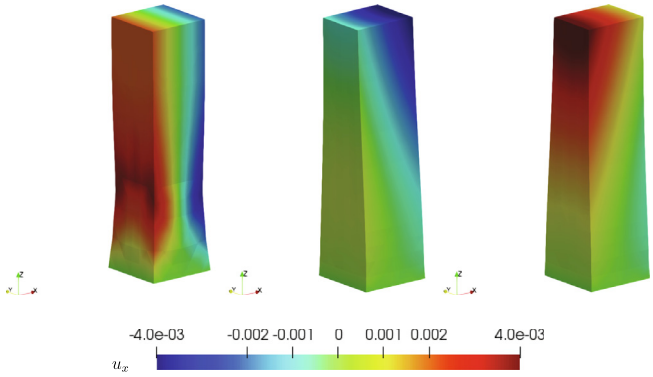

Fig. 10. Perspective view of displacement in *x*-direction on deformed solid: Orientation 1 (left), orientation 2 (middle), orientation 3 (right).

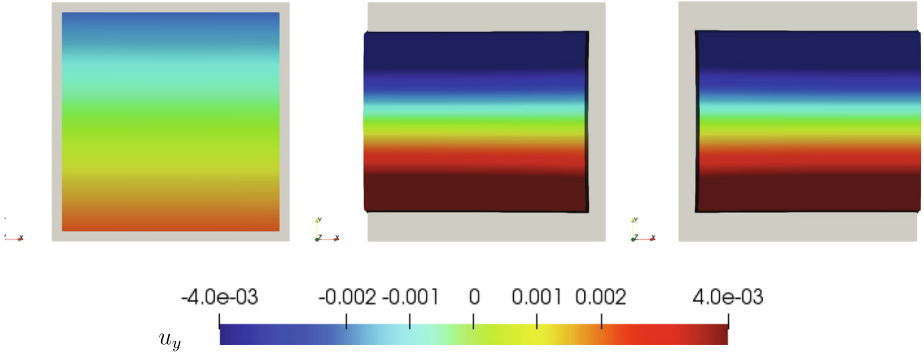

Fig. 9. Top view of displacement in *y*-direction on deformed solid. The initial shape of the solid is shown in grey: Orientation 1 (left), orientation 2 (middle), orientation 3 (right).

Fig. 10 shows the displacement in x-direction in a perspective view and reveals the arising shear bands in the deformed solid of orientation 2 and 3. No such shear bands can be seen for orientation 1. Note that the shear bands arises solely from the orientation of the crystal, no imperfection has been introduced.

6. Conclusion

The present work discusses different tangent operator formulations for a single crystal plasticity algorithm based on the infeasible primal–dual interior point method, which has been first presented in Scheunemann et al. (2020). In addition to the algorithmic tangent moduli, a numerical differentiation scheme based on a perturbation along the imaginary axis, following Tanaka et al. (2014), is used to compute the tangent moduli and the element stiffness matrix. In the comparison of a monocrystalline structure under uniaxial extension, the different tangent formulations are compared regarding their convergence behavior. It must be noted that no formulation led to quadratic convergence of the norm of the residual of the finite element formulation. Whereas the algorithms based on the CSDA scheme lead to faster convergence, the algorithmic tangent here still lead to faster simulations due to the lower number of evaluations of the local algorithm based on the infeasible primal–dual interior point method, which requires to solve a sequence of Newton schemes with decreasing barrier parameter. The observed non-quadratic convergence behavior of the solution based on the algorithmic tangent may arise from the computation of the inverse matrices of possibly ill-conditioned matrices and the summation operation during the matrix multiplication to compute $\boldsymbol{C}_{\text{fact}}$. Small deficiancies in this matrix due to poor inversion of the matrices lead to larger differences in the final tangent moduli. A possibility to overcome this problem could be the construction of a dimensionless formulation of the Lagrangian function.

The algorithmic tangent formulation is used to evaluate the numerical example under varying orientation of the underlying monocrystal. Thereby, an orientation-specific forming of shear bands in the solid can be shown when the crystal is rotated out of its intial orientation. The observed shear bands arise from the initial orientation of the crystal, no initial imperfection has been included.

Declaration of Competing Interest

The authors declare that they have no known competing financial interests or personal relationships that could have appeared to influence the work reported in this paper.

Appendix A

A.1. Algorithmic consistent material tangent

First formulation

Following from the formulation of the Schur complement in Scheunemann et al. (2020), one obtains for the increment of the plastic slip

$$\Delta\Delta\boldsymbol{\gamma} = \left[\boldsymbol{H}_{11} - \boldsymbol{H}_{12}\boldsymbol{H}_{22}^{-1}\boldsymbol{H}_{21}\right]^{-1}\left[\boldsymbol{r}_1 - \boldsymbol{H}_{12}\boldsymbol{H}_{22}^{-1}\boldsymbol{r}_2\right]. \tag{84}$$

We seek the derivative

$$\frac{\partial\Delta\boldsymbol{\gamma}_{n+1}}{\partial\boldsymbol{\varepsilon}_{n+1}} = \frac{\partial\Delta\boldsymbol{\gamma}_{n+1}}{\partial\bar{b}_1}\frac{\partial\bar{b}_1}{\partial\boldsymbol{\varepsilon}_{n+1}} = \left[\boldsymbol{H}_{11} - \boldsymbol{H}_{12}\boldsymbol{H}_{22}^{-1}\boldsymbol{H}_{21}\right]^{-1}\frac{\partial\bar{b}_1}{\partial\boldsymbol{\varepsilon}_{n+1}} \tag{85}$$

$$\frac{\partial\bar{b}_1}{\partial\boldsymbol{\varepsilon}_{n+1}} = \frac{\partial\left[\boldsymbol{r}_1 - \boldsymbol{H}_{12}\boldsymbol{H}_{22}^{-1}\boldsymbol{r}_2\right]}{\partial\boldsymbol{\varepsilon}_{n+1}} = \frac{\partial\boldsymbol{r}_1}{\partial\boldsymbol{\varepsilon}_{n+1}} - \boldsymbol{H}_{12}\boldsymbol{H}_{22}^{-1}\frac{\partial\boldsymbol{r}_2}{\partial\boldsymbol{\varepsilon}_{n+1}} \tag{86}$$

with

$$\boldsymbol{r}_1 = -\frac{\partial\boldsymbol{D}}{\partial\Delta\boldsymbol{\gamma}} - \frac{\partial\boldsymbol{\Phi}}{\partial\Delta\boldsymbol{\gamma}}\boldsymbol{\lambda} + \mu\Delta\boldsymbol{\Gamma}^{-1}\boldsymbol{e} \qquad \text{and} \qquad \boldsymbol{r}_2 = -\boldsymbol{\Phi} - \mu\boldsymbol{\Lambda}^{-1}\boldsymbol{e}. \tag{87}$$

Using the derivative

$$\frac{\partial\bar{b}_1}{\partial\boldsymbol{\varepsilon}_{n+1}} = -\underline{\boldsymbol{P}}\,\underline{\mathbb{C}}^{\text{e}} + \boldsymbol{H}_{12}\boldsymbol{H}_{22}^{-1}\underline{\boldsymbol{P}}\,\underline{\mathbb{C}}^{\text{e}} \tag{88}$$

leads to

$$\begin{aligned}\frac{\partial\Delta\gamma_{n+1}}{\partial\boldsymbol{\varepsilon}_{n+1}} &= \left[\boldsymbol{H}_{11} - \boldsymbol{H}_{12}\boldsymbol{H}_{22}^{-1}\boldsymbol{H}_{21}\right]^{-1}\left[-\underline{\boldsymbol{P}}\,\underline{\mathbb{C}}^{\text{e}} + \boldsymbol{H}_{12}\boldsymbol{H}_{22}^{-1}\underline{\boldsymbol{P}}\,\underline{\mathbb{C}}^{\text{e}}\right]\\ &= \left[\boldsymbol{H}_{11} - \boldsymbol{H}_{12}\boldsymbol{H}_{22}^{-1}\boldsymbol{H}_{21}\right]^{-1}\left[-\boldsymbol{I} + \boldsymbol{H}_{12}\boldsymbol{H}_{22}^{-1}\right]\underline{\boldsymbol{P}}\,\underline{\mathbb{C}}^{\text{e}}\\ &= \left(-\left[\boldsymbol{H}_{11} - \boldsymbol{H}_{12}\boldsymbol{H}_{22}^{-1}\boldsymbol{H}_{21}\right]^{-1} + \left[\boldsymbol{H}_{11} - \boldsymbol{H}_{12}\boldsymbol{H}_{22}^{-1}\boldsymbol{H}_{21}\right]^{-1}\left[\boldsymbol{H}_{12}\boldsymbol{H}_{22}^{-1}\right]\right)\underline{\boldsymbol{P}}\,\underline{\mathbb{C}}^{\text{e}}\\ &= \boldsymbol{C}_{\text{fact}}\underline{\boldsymbol{P}}\,\underline{\mathbb{C}}^{\text{e}}\end{aligned} \tag{89}$$

with

$$\begin{aligned}\boldsymbol{H}_{11} &= -\tfrac{\partial^2 D}{\partial\Delta\gamma^2} + \tfrac{\partial^2\boldsymbol{\Phi}}{\partial\Delta\gamma^2}\boldsymbol{\lambda} + \mu\boldsymbol{\Gamma}^{-2}\\ &= 2\,\underline{\boldsymbol{P}}^T\,\underline{\mathbb{C}}^{\text{e}}\,\underline{\boldsymbol{P}} - \tfrac{\partial^2\boldsymbol{g}}{\partial\Delta\gamma^2}\Delta\boldsymbol{\gamma} - 2\,\tfrac{\partial\boldsymbol{g}}{\partial\Delta\gamma} - \tfrac{\partial^2\boldsymbol{g}}{\partial\Delta\gamma^2}\boldsymbol{\lambda} + \mu\boldsymbol{\Gamma}^{-2}\\ \boldsymbol{H}_{12} &= \tfrac{\partial\boldsymbol{\Phi}^T}{\partial\Delta\boldsymbol{\gamma}} = -\underline{\boldsymbol{P}}\,\underline{\mathbb{C}}^{\text{e}}\,\underline{\boldsymbol{P}}^T - \tfrac{\partial\boldsymbol{g}^T}{\partial\Delta\boldsymbol{\gamma}}\\ \boldsymbol{H}_{21} &= \tfrac{\partial\boldsymbol{\Phi}}{\partial\Delta\boldsymbol{\gamma}} = -\underline{\boldsymbol{P}}^T\,\underline{\mathbb{C}}^{\text{e}}\,\underline{\boldsymbol{P}} - \tfrac{\partial\boldsymbol{g}}{\partial\Delta\boldsymbol{\gamma}}\\ \boldsymbol{H}_{22} &= -\boldsymbol{\Lambda}^{-1}\boldsymbol{S}.\end{aligned} \tag{90}$$

Second tangent formulation

From the Schur complement, one obtains

$$\Delta\boldsymbol{\lambda} = \left[\boldsymbol{H}_{22} - \boldsymbol{H}_{21}\boldsymbol{H}_{11}^{-1}\boldsymbol{H}_{12}\right]^{-1}\left[\boldsymbol{r}_2 - \boldsymbol{H}_{21}\boldsymbol{H}_{11}^{-1}\boldsymbol{r}_1\right] \tag{91}$$

which is substituted into

$$\Delta\boldsymbol{\gamma} = \boldsymbol{H}_{11}^{-1}\left[\boldsymbol{r}_1 - \boldsymbol{H}_{12}\left(\left[\boldsymbol{H}_{22} - \boldsymbol{H}_{21}\boldsymbol{H}_{11}^{-1}\boldsymbol{H}_{12}\right]^{-1}\left[\boldsymbol{r}_2 - \boldsymbol{H}_{21}\boldsymbol{H}_{11}^{-1}\boldsymbol{r}_1\right]\right)\right] \tag{92}$$

and reformulated as

$$\begin{aligned}\Delta\boldsymbol{\gamma} = &\left(\boldsymbol{H}_{11}^{-1} + \boldsymbol{H}_{11}^{-1}\boldsymbol{H}_{12}\left[\boldsymbol{H}_{22} - \boldsymbol{H}_{21}\boldsymbol{H}_{11}^{-1}\boldsymbol{H}_{12}\right]^{-1}\boldsymbol{H}_{21}\boldsymbol{H}_{11}^{-1}\right)\boldsymbol{r}_1\\ &-\left(\boldsymbol{H}_{11}^{-1}\boldsymbol{H}_{12}\left[\boldsymbol{H}_{22} - \boldsymbol{H}_{21}\boldsymbol{H}_{11}^{-1}\boldsymbol{H}_{12}\right]^{-1}\right)\boldsymbol{r}_2\end{aligned} \tag{93}$$

With the above mentioned derivations one obtains in this case

$$\begin{aligned}\frac{\partial\Delta\gamma_{n+1}}{\partial\boldsymbol{\varepsilon}_{n+1}} &= \frac{\partial\Delta\gamma_{n+1}}{\partial\boldsymbol{r}_1}\frac{\partial\boldsymbol{r}_1}{\partial\boldsymbol{\varepsilon}_{n+1}} + \frac{\partial\Delta\gamma_{n+1}}{\partial\boldsymbol{r}_2}\frac{\partial\boldsymbol{r}_2}{\partial\boldsymbol{\varepsilon}_{n+1}}\\ &= \left(\boldsymbol{H}_{11}^{-1} + \boldsymbol{H}_{11}^{-1}\boldsymbol{H}_{12}\left[\boldsymbol{H}_{22} - \boldsymbol{H}_{21}\boldsymbol{H}_{11}^{-1}\boldsymbol{H}_{12}\right]^{-1}\boldsymbol{H}_{21}\boldsymbol{H}_{11}^{-1}\right)\frac{\partial\boldsymbol{r}_1}{\partial\boldsymbol{\varepsilon}_{n+1}}\\ &-\left(\boldsymbol{H}_{11}^{-1}\boldsymbol{H}_{12}\left[\boldsymbol{H}_{22} - \boldsymbol{H}_{21}\boldsymbol{H}_{11}^{-1}\boldsymbol{H}_{12}\right]^{-1}\right)\frac{\partial\boldsymbol{r}_2}{\partial\boldsymbol{\varepsilon}_{n+1}}\\ &= -\overline{\boldsymbol{H}_1}\underline{\boldsymbol{P}}\,\underline{\mathbb{C}}^{\text{e}} + \overline{\boldsymbol{H}_2}\underline{\boldsymbol{P}}\,\underline{\mathbb{C}}^{\text{e}}\\ &= (\overline{\boldsymbol{H}}_2 - \overline{\boldsymbol{H}}_1)\underline{\boldsymbol{P}}\,\underline{\mathbb{C}}^{\text{e}}\end{aligned} \tag{94}$$

where

$$\overline{\boldsymbol{H}_1} = \left(\boldsymbol{H}_{11}^{-1} + \boldsymbol{H}_{11}^{-1}\boldsymbol{H}_{12}\left[\boldsymbol{H}_{22} - \boldsymbol{H}_{21}\boldsymbol{H}_{11}^{-1}\boldsymbol{H}_{12}\right]^{-1}\boldsymbol{H}_{21}\boldsymbol{H}_{11}^{-1}\right) \tag{95}$$

and

$$\overline{\boldsymbol{H}}_2 = \left(\boldsymbol{H}_{11}^{-1} \boldsymbol{H}_{12} \left[\boldsymbol{H}_{22} - \boldsymbol{H}_{21} \boldsymbol{H}_{11}^{-1} \boldsymbol{H}_{12} \right]^{-1} \right) \tag{96}$$

A.2. Complementary condition of slip rates

In primal–dual interior point methods, the formulation of a constrained optimization problem given by

$$\text{minimize} \quad f(x) \quad \text{subject to} \quad g(x) \geqslant 0 \tag{97}$$

can be derived from the formulation of a logarithmic barrier method

$$\text{minimize} \quad \beta_\mu(x) = f(x) - \mu \ln(g(x)) \tag{98}$$

which is solved for a decreasing sequence of barrier parameters μ. Setting the gradient of the barrier function to zero, one obtains

$$\begin{aligned} &\nabla f(x) - \mu \tfrac{\nabla g(x)}{g(x)} = 0 \\ \leftrightarrow\ &\nabla f(x) - \tfrac{\mu}{g(x)} \nabla g(x) = 0 \\ \leftrightarrow\ &\nabla f(x) - \lambda_g \nabla g(x) = 0 \end{aligned} \tag{99}$$

with the Lagrange multiplier $\lambda_g(\mu) = \frac{\mu}{g(x)}$. Following Griva et al. (2009), the solution of the barrier problem is then also the solution of the perturbed primal–dual system of equations given by

$$\begin{aligned} g(x) &\geqslant 0 \\ \nabla_x L(x, \lambda) = \nabla f(x) - \lambda_g \nabla g(x) &= 0 \\ \lambda_g &\geqslant 0 \\ \lambda_g g(x) &= \mu \end{aligned} \tag{100}$$

with the Lagrangian of the problem being

$$L(x, \lambda) = f(x) - \lambda_g \, g(x). \tag{101}$$

For this primal dual problem, in the classical primal–dual interior point sense, the Newton directions $(\Delta x, \Delta \lambda_g)$ can be found using a Taylor series ignoring terms of second and higher order, leading to

$$\begin{bmatrix} \nabla^2_{xx} L(x, \lambda) & -\nabla g(x) \\ \lambda_g \, g(x) & g(x) \end{bmatrix} \begin{bmatrix} \Delta x \\ \Delta \lambda_g \end{bmatrix} = \begin{bmatrix} \nabla_x L(x, \lambda) \\ -\lambda_g \, g(x) + \mu \end{bmatrix}, \tag{102}$$

$$\begin{bmatrix} \nabla^2 f(x) - \lambda_g \nabla^2 g(x) & -\nabla g(x) \\ \lambda_g \, g(x) & g(x) \end{bmatrix} \begin{bmatrix} \Delta x \\ \Delta \lambda_g \end{bmatrix} = \begin{bmatrix} \nabla_x L(x, \lambda) \\ -\lambda_g \, g(x) + \mu \end{bmatrix}. \tag{103}$$

This consideration of the Lagrange multiplier λ_g leads to additional equations which need to be solved when a primal–dual formulation is considered. Opposed to this, a purely primal formulation is obtained considering the linearization of the gradient of Eq. (99), leading to

$$\left(\nabla^2_{xx} f(x) + \mu \frac{\nabla^2 g(x)}{(g(x))^2} \nabla g(x) \right) \Delta x = \nabla f(x) - \mu \frac{\nabla g(x)}{g(x)}. \tag{104}$$

A reformulation of the second line of Eq. (103) with respect to $\Delta \lambda_g$, i.e.,

$$\Delta \lambda = \frac{1}{g(x)} \left(-\lambda_g \, g(x) + \mu - \lambda_g \nabla g(x) \Delta x \right) \tag{105}$$

and inserting into the first equation yields

$$\rightarrow \nabla^2_{xx} L(x, \lambda) \Delta x + \frac{\lambda_g}{g(x)} \nabla g(x) \Delta x = -\nabla_x L - \lambda + \frac{\mu}{g(x)} \tag{106}$$

and the Lagrange multiplier is updated by

$$\lambda_g \leftarrow \lambda_g + \Delta \lambda_g, \quad \Delta \lambda_g = -\lambda_g + \frac{\mu}{g(x)} - \frac{\lambda_g \nabla g(x)}{g(x)} \Delta x. \tag{107}$$

Note that from Eq. (108), it can be seen that when the primal variable converges, i.e. $\Delta x \to 0$, the complementary condition related to x, meaning $\lambda_g = \mu / g(x)$ is fulfilled and $\Delta \lambda_g \to 0$ converges.

The above formulation enables the possibility to consider the Lagrange multiplier to the constraint condition on the problem without introducing the additional equation in the equation system directly. In the application of the above described reformulation in the infeasible primal dual interior point method to the problem of crystal plasticity, this has the advantage of having a natural perturbation applied on the ill-conditioned Hessian of the original problem, since the part of the hessian associated to $\boldsymbol{\gamma}$ is ill-conditioned, which was also discussed in Scheunemann et al. (2020). From the consideration of the Lagrange multiplier associated to the constraint $\boldsymbol{\gamma} \geqslant 0$, a fully primal–dual formulation is obtained, which is generally more stable than primal formulations, compare Griva et al. (2009).

The Lagrange multiplier and the related complementary condition resulting from Eq. (13.3) can be considered in analogy to the above described example. The complementary condition then reads

$$\boldsymbol{\rho}_\gamma \boldsymbol{\gamma} = \boldsymbol{\mu}, \tag{108}$$

where $\boldsymbol{\rho}_\gamma$ is the Lagrange multiplier, thus the dual variable arising from the constraint $\dot{\boldsymbol{\gamma}} \geqslant \boldsymbol{0}$. For the system of equations to compute the Newton directions, the above described handling results in the modification

$$\begin{bmatrix} 2\underline{\boldsymbol{P}}^T \underline{\mathbb{C}}^{\mathrm{e}} \underline{\boldsymbol{P}} - \boldsymbol{H}(\boldsymbol{\gamma}) - \frac{\partial^2 \boldsymbol{g}}{\partial \Delta \boldsymbol{\gamma}^2} \boldsymbol{\lambda} + \boldsymbol{\Theta}_\gamma \Delta \boldsymbol{\Gamma}^{-1} & -\underline{\boldsymbol{P}}^T \underline{\mathbb{C}}^{\mathrm{e}} \underline{\boldsymbol{P}} - \frac{\partial \boldsymbol{g}}{\partial \Delta \boldsymbol{\gamma}}^T \\ \left(-\underline{\boldsymbol{P}}^T \underline{\mathbb{C}}^{\mathrm{e}} \underline{\boldsymbol{P}} - \frac{\partial \boldsymbol{g}}{\partial \Delta \boldsymbol{\gamma}}^T \right)^T & -\boldsymbol{\Lambda}^{-1} \boldsymbol{S} \end{bmatrix} \begin{bmatrix} \Delta \Delta \boldsymbol{\gamma} \\ \Delta \boldsymbol{\lambda} \end{bmatrix} = \dots$$
$$\begin{bmatrix} \boldsymbol{P}^T \underline{\mathbb{C}}^{\mathrm{e}} \underline{\boldsymbol{\varepsilon}}^{\mathrm{e,trial}} - 2\boldsymbol{P}^T \underline{\mathbb{C}}^{\mathrm{e}} \underline{\boldsymbol{P}} \Delta \boldsymbol{\gamma} + \boldsymbol{h}(\Delta \boldsymbol{\gamma}) + \left[\boldsymbol{P}^{\mathrm{T}} \underline{\mathbb{C}}^{\mathrm{e}} \underline{\boldsymbol{P}} + \frac{\partial \boldsymbol{g}}{\partial \Delta \boldsymbol{\gamma}} \right] \boldsymbol{\lambda} + \boldsymbol{\rho}_\gamma - \boldsymbol{\rho}_\gamma + \mu \boldsymbol{\Gamma}^{-1} \boldsymbol{e}_m \\ -\boldsymbol{P}^T \underline{\mathbb{C}}^{\mathrm{e}} \left[\underline{\boldsymbol{\varepsilon}}^{\mathrm{e,trial}} - \underline{\boldsymbol{P}} \Delta \boldsymbol{\gamma} \right] + \boldsymbol{g}_{n+1} - \mu \boldsymbol{\Lambda}^{-1} \boldsymbol{e}_m \end{bmatrix} \tag{109}$$

where the update of the Lagrange multiplier needs to be considered with

$$\boldsymbol{\rho}_\gamma \leftarrow \boldsymbol{\rho}_\gamma + \Delta \boldsymbol{\rho}_\gamma = \mu \Delta \boldsymbol{\Gamma}^{-1} \boldsymbol{e}_m - \boldsymbol{\Theta}_\gamma \Delta \boldsymbol{\Gamma}^{-1} \Delta \Delta \boldsymbol{\gamma} \tag{110}$$

with $\boldsymbol{\Theta}_\gamma = \mathrm{diag}\left(\boldsymbol{\rho}_\gamma \right)$. This treatment stabilizes the algorithm due to the fully primal–dual treatment and can be seen as a damping on the fulfillment of $\boldsymbol{\Theta}_\gamma \boldsymbol{\gamma} \to \boldsymbol{0}$ as $\mu \to 0$.

References

Alberty, J., Carstensen, C., Zarrabi, D., 1999. Adaptive numerical analysis in primal elastoplasticity with hardening. Computer Methods Appl. Mech. Eng. 171, 175–204.

Anand, L., Kothari, M., 1996. A complasticity procedure for rate-independent crystal plasticity. J. Mech. Phys. Solids 44, 525–558.

Arminjon, M., 1991. A regular form of the Schmid law. Application to the ambiguity problem. Textures Microstructures 14–18, 1121–1128.

Asaro, R.J., 1983. Crystal plasticity. Trans. ASME 50, 921–934.

Asaro, R.J., Rice, J.R., 1977. Strain localization in ductile single crystals. J. Mech. Phys. Solids 25, 309–338.

Blaheta, R., 1997. Convergence of newton-type methods in incremental return mapping analysis of elasto-plastic problems. Computer Methods Appl. Mech. Eng. 147, 167–185.

Borja, R.I., Rahmani, H., 2012. Computational aspects of elasto-plastic deformation in polycrystalline solids. J. Appl. Mech. 79 (3). 031024–031024–9.

Borja, R.I., Wren, J.R., 1993. Discrete micromechanics of elastoplastic crystals. Int. J. Numer. Meth. Eng. 36, 3815–3840.

Busso, E.P., Cailletaud, G., 2005. Selection of active slip systems in crystal plasticity. Int. J. Plast 21, 2212–2231.

Chang, Y.W., Asaro, R.J., 1981. An experimental study of shear localization in aluminum-copper single crystals. Acta Metall. 29, 241–257.

Cuitiño, A.M., Ortiz, M., 1992. Computation modelling of single crystals. Modelling Simul. Mater. Sci. Eng. 1, 225–263.

Forest, S., Gueninchault, N., 2013. Inspection of free energy functions in gradient crystal plasticity. Acta. Mech. Sin. 29 (6), 763–772.

Gambin, W., 1992. Refined analysis of elastic-plastic crystals. Int. J. Solids Struct. 29 (16), 2013–2021.

Griva, I., Nash, S.G., Sofer, A., 2009. Linear and Nonlinear Optimization,. SIAM.
Gurtin, M.E., 2000. On the plasticity of single crystals: free energy, microforces, plastic-strain gradients. J. Mech. Phys. Solids 48 (5), 989–1036.
Gurtin, M.E., Anand, L., Lele, S.P., 2007. Gradient single-crystal plasticity with free energy dependent on dislocation densities. J. Mech. Phys. Solids 55, 1853–1878.
Havner, K.S., 1982. The theory of finite plastic deformation of crystalline solids. In: Hopkins, H.G., Sewell, M.J. (Eds.), Mechanics of Solids. The Rodnes Hill 60th anniversary volume. Pergamon Press, Oxford, pp. 265–302.
Hinder, O., Ye, Y. 2018. A one-phase interior point method for nonconvex optimization. arXiv:1801.03072v2, pages 1–30, 2018..
Hürkamp, A., Tanaka, M., Kaliske, M., 2015. Complex-step derivative approximation of consistent tangent operators for viscoelasticity based on fractional calculus. Comput. Mech. 56, 1055–1071.
Hutchinson, J.W., 1976. Bounds and self-consistent estimates for creep of polycrystalline materials. Proc. R. Soc. Lond. A. 348, 101–127.
Kim, S., Ryu, J., Cho, M., 2011. Numerically generated tangent stiffness matrices using the complex variable derivative method for nonlinear structural analysis. Computer Methods Appl. Mech. Eng. 200 (1), 403–413.
Kocks, U.F., 1970. The relation between polycrystalline deformation and single crystal deformation. Metall. Trans. 1, 1121–1142.
Koiter, W.T., 1960. General theorems of elasto-plastic deformation of crystalline solids. In: Sneddon, I.N., Hill, R. (Eds.), Progress in Solid Mechanics. North-Holland, Amsterdam.
Lai, K.-L., Crassidis, J.L., 2008. Extensions of the frirst and second complex-step derivative approximations. J. Comput. Appl. Math. 219, 276–293.
Lewandowski, M.J., Stupkiewicz, S., 2018. Size effects in wedge indentation predicted by a gradient-enhanced crystal-plasticity model. Int. J. Plast 109, 54–78.
Lyness, J.N., 1968. Differentiation formulas for analytical functions. Math. Comput. 22, 352–362.
Mandel, J., 1972. Plasticité classique et viscoplasticité. CISM course, Nr. 97. Springer.
Mathur, K.K., Dawson, P.R., 1989. On modeling the development of crystallographic texture in bulk forming processes. Int. J. Plast 5, 67–94.
McGinty, R.D., McDowell, D.L., 2006. A semi-implicit integration scheme for rate independent finite crystal plasticity. Int. J. Plast 22, 996–1025.
Miehe, C., 1996. Exponential map algorithm for stress updates in anisotropic multiplicative elastoplasticity for single crystals. Int. J. Numer. Meth. Eng. 39, 3367–3390.
Miehe, C., Rosato, D., 2007. Fast texture updates in fcc polycrystal plasticity based on a linear active-set-estimate of the lattice spin. J. Mech. Phys. Solids 55, 2687–2716.
Miehe, C., Schröder, J., 2001. A comparative study of stress update algorithms for rate independent and rate dependent crystal plasticity. Int. J. Numer. Meth. Eng. 50, 273–298.
Nigro, P.S.B., Simões, E.T., Pimenta, P.M., Schröder, J., 2019. Model order reduction with galerkin projection applied to nonlinear optimization with infeasible primal-dual interior point method. Int. J. Numer. Meth. Eng. 120 (12), 1310–1348.
Ortiz, M., Stainier, L., 1999. The variational formulation of viscoplastic constitutive updates. Computer Methods Appl. Mech. Eng. 171, 419–444.
Peirce, D., Asaro, R.J., Needleman, A., 1982. An analysis of nonlinear and localized deformation in ductile single crystals. Acta Metall. 30, 1087–1119.
Pérez-Foguet, A., Rodríguez-Ferran, A., Huerta, A., 2000. Numerical differentiation for local and global tangent operators in computational lasticity. Computer Methods Appl. Mech. Eng. 189, 277–296.
Pérez-Foguet, A., Rodríguez-Ferran, A., Huerta, A., 2000. Numerical differentiation for nontrivial consistent tangent matrices: an application to the MRS-lade model. Int. J. Numer. Meth. Eng. 48, 159–184.
Prüger, S., Kiefer, B., 2020. A comparative study of integration algorithms for finite single crystal (visco-)plasticity. Int. J. Mech. Sci. 180, 105740.
Reddy, B.D., Wieners, C., Wohlmuth, B., 2012. Finite element analysis and algorithms for single crystal strain-gradient plasticity. Int. J. Numer. Meth. Eng. 90, 784–804.
Roters, F., Eisenlohr, P., Bieler, T.R., Raabe, D., 2010. Crystal Plasticity Finite Element Methods in Materials Science and Engineering. Wiley-VCH, Weinheim.
Sauter, M., Wieners, C., 2011. On the superlinear convergence in computational elasto-plasticity. Computer Methods Appl. Mech. Eng. 200, 3646–3658.
Scheunemann, L., Schröder, J., Nigro, P.S.B., Pimenta, P.M., 2020. A novel algorithm for rate independent small strain crystal plasticity based on the infeasible primal-dual interior point method. Int. J. Plast 124, 1–19.
Schmidt-Baldassari, M., 2003. Numerical concepts for rate-independent single crystal plasticity. Computer Methods Appl. Mech. Eng. 192, 1261–1280.
Schröder, J., Miehe, C., 1997. Aspects of computational rate-independent crystal plasticity. Comput. Mater. Sci. 9, 168–176.
Shanthraj, P., Eisenlohr, P., Diehl, M., Roters, F., 2015. Numerical robust spectral method for crystal plasticity simulations of heterogeneous materials. Int. J. Plast 66, 31–45.
Simo, J.C., 1998. Numerical analysis and Simulation of Plasticity. Elsevier Science B. V..
Simo, J.C., Kennedy, J.G., Govindjee, S., 1988. Non-smooth multisurface plasticity and viscoplasticity. loading/unloading ccondition and numerical algorithms. Int. J. Numer. Meth. Eng. 26, 2161–2185.
Steinmann, P., Stein, E., 1996. On the numerical treatment and analysis of finite deformation ductile single crystal plasticity. Computer Methods Appl. Mech. Eng. 129, 235–254.
Sun, W., Chaikof, E.L., Levenston, M.E., 2008. Numerical approximation of tangent moduli for finite element implementations of nonlinear hyperelastic material models. J. Biomech. Eng. 130, 061003.
Tanaka, M., Balzani, D., Schröder, J., 2016. Implementation of incremental variational formulations based on the numerical calculation of derivatives using hyper dual numbers. Computer Methods Appl. Mech. Eng. 301, 216–241.
Tanaka, M., Fujikawa, M., Balzani, D., Schröder, J., 2014. Robust numerical calculation of tangent moduli at finite strains based on complex-step derivative approximation and its application to localization analysis. Computer Methods Appl. Mech. Eng. 269, 454–470.
Taylor, G.I., 1938. Plastic strains in metals. J. Institute Metals 62, 307–324.
Wulfinghoff, S., Böhlke, T., 2013. Equivalent plastic strain gradient crystal plasticity - enhanced power law subroutine. Gamm Mitteilungen 36 (2), 134–148.
Wulfinghoff, S., Böhlke, T., 2015. Gradient crystal plasticity including dislocation-based ork hardening dislocation transport. Int. J. Plast 69, 152–169.
Zuo, Q.H., 2011. The uniqueness of a rate-independent plasticity model for single crystal. Int. J. Plast 27, 1145–1164.